Generation of vortex beam superpositions using angular gratings

Marie-Claude Dicaire

Thesis submitted to the
Faculty of Graduate and Postdoctoral Studies
in partial fulfillment of the requirements
for the M.Sc. degree in Physics

Ottawa-Carleton Institute of Physics
Department of Physics
Faculty of Science
University of Ottawa
Ottawa, Canada

Abstract

Beams of light carrying orbital angular momentum, such as vortex beams, have many applications in imaging and micromanipulation. We focus on applications in communication, in particular for quantum key distribution, where the security of communication channels is enhanced with the laws of quantum mechanics. However, this procedure requires superpositions of vortex beams. We want to generate such beams using integrated optics components due to their small size and their advantages in scalability and stability.

Angular gratings, which are ring resonators with an embedded Bragg grating, are integrated structures known to generate vortex beams. We propose that a ring resonator with two embedded Bragg gratings, each on the inner and outer sidewalls, would generate a superposition of vortex beams. We verify this claim through analytical models, simulations and experiments.

Résumé

Les faisceaux de lumière avec un moment cinétique orbital, tels les faisceaux vortex, ont plusieurs applications en imagerie et en micromanipulation. Nous nous concentrons sur les applications en communication, en particulier en distribution quantique de clés où la sécurité de canaux de communication est renforcée par les lois de la méchanique quantique. Cependant, cette procédure exige des superpositions de faisceaux vortex. Nous voulons générer de tels faisceaux en utilisant des composantes optiques intégrées en raison de leur petite taille et de leurs avantages en adaptabilité et stabilité.

On sait que les réseaux de diffractions angulaires, qui sont des résonateurs en anneau avec un réseau de Bragg incorporé, sont des structures intégrées qui génèrent des faisceaux vortex. Nous proposons qu'un résonateur en anneau avec deux réseaux de Bragg incorporés, chacun sur les côtés intérieur et extérieur de l'anneau, génèrerait une superposition de faisceaux vortex. Nous vérifions cette affirmation à travers des modèles analytiques, des simulations et des expériences.

Acknowledgements

First, I would like to thank my supervisor Prof. Robert Boyd for his advice and the opportunities given throughout my Master's degree.

I want to also thank our lab manager Dr. Jeremy Upham and post-doc Dr. Sebastian Schulz, who have both been involved in this project from beginning to end, for the many discussions and advice, the fabrication of the nanostructures and reading my thesis. Their help was significant in the achievement of this thesis. I would like to also thank Dr. Liam O'Faolain at the University of St Andrews for etching our nanostructures.

I acknowledge the financial support of the Canada Excellence Research Chairs (CERC) program, the Natural Sciences and Engineering Research Council of Canada (NSERC) and the Ontario Graduate Scholarship (OGS) program.

Finally, I want to thank my family and friends for their support throughout my studies and making this time an enjoyable experience.

Table of Contents

List of Figures

1. Introduction

Optical vortices describes a phase front of light that twists into a phase singularity. To be physical, the undefined phase spot has to carry zero intensity [1]. A beam containing an optical vortex on its propagation axis is thus called a vortex beam, or "doughnut beam" as it is characterized by a hollow centre. In order to create this phase twist, the direction of each light ray forming the vortex beam has to be slanted in a way such that their tranversal components form a circle rotating in one direction. This momentum in the transversal plane leads to orbital angular momentum (OAM), and so we can say that vortex beams carry OAM.

In this chapter, we will provide a description of the OAM in light and review the main applications and methods of generation of vortex beams. The application in which we are most interested involves the security of communication, which requires beams in a superposition of OAM states [2]. At the same time, numerous ways of generating vortex beams already exist but few can be mass-produced or have a size as small as a few tens of microns. Our main goal is thus to generate superpositions of vortex beams in a way that is scalable, reliable and to facilitate integration. Our chosen method is an angular grating [3], an integrated ring resonator with an embedded Bragg grating, as the light scattering out of the grating directly over the slab forms a vortex beam. The purpose of this thesis is to show, through theory, simulations and experiments, that a single ring resonator with two embedded grating generates a superposition of vortex beams.

1.1. Orbital angular momentum of light

It has long been known that light possesses linear momentum. As early as 1619, Johannes Kepler noticed that the tail of comets always points in the direction opposite to the sun, a result of radiation pressure giving away the momentum property of light [4]. The linear momentum of light is proportional to its wave vector $\mathbf{k} = 2\pi/\lambda\,\hat{\mathbf{k}}$ where λ is the wavelength

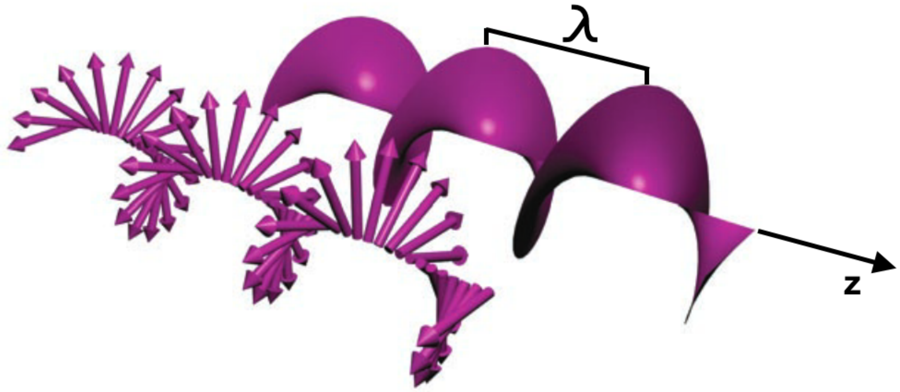

Figure 1.1.: The spin angular momentum (SAM), on the left, is a vector quantity tied to the polarization of light as the polarization vector precesses around the propagation axis. The orbital angular momentum (OAM), on the right, is a scalar quantity tied to the phase front of light. Here, it is the trajectory of a point of constant phase that precesses around the propagation axis. Based on [5].

and $\hat{\mathbf{k}}$ is a unit vector in direction of the phase velocity. Akin to mechanical systems, light also has spin angular momentum (SAM) and orbital angular momentum (OAM). While both angular momenta describe a rotation in light, it is important to make the distinction between the two. Their differences are represented in Fig. 1.1.

On the one hand, SAM is a vector quantity related to the polarization of the light. Its basis is made of the left and right circular polarizations with the associated SAM of $\pm\hbar$ for a single photon, where $\hbar$ is Planck's constant divided by 2π. The sign of the SAM depends on the convention used.

On the other hand, OAM is a scalar quantity describing the helical structure of the phase front, or how much the light "twists" around its optical axis, as demonstrated in Fig. 1.2. Because of this twisting nature, this kind of beam is called vortex beam. Analytically, the OAM appears in the electric field equation with a factor of $e^{il\phi}$, where l is an integer labelling the OAM state [6] and ϕ is the azimuthal angle on a plane transverse to the propagation axis. The number of OAM states is infinite and they are all orthogonal to each other. Since the phase is periodic with the azimuthal angle, the phase on the propagation axis is undefined and the intensity is null. This creates a ring pattern in intensity and is why a vortex beam is also called a "doughnut beam". Although it is easier to visualize

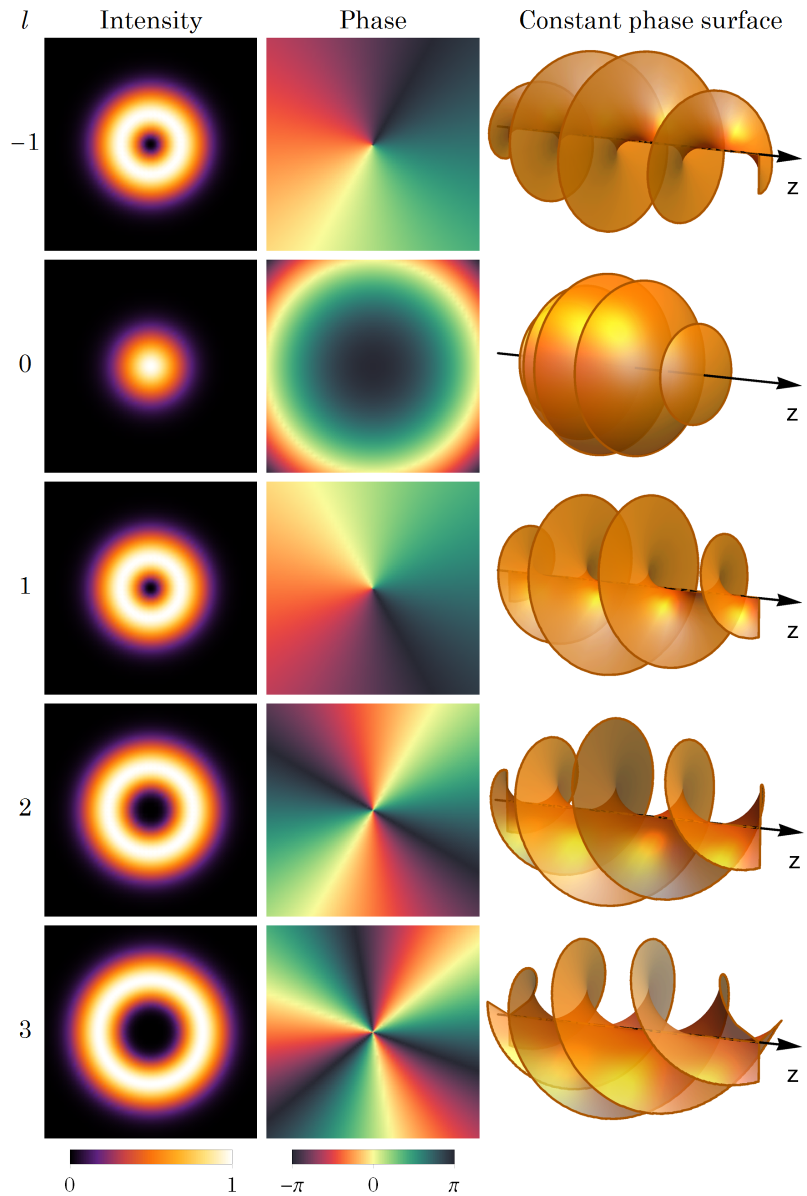

Figure 1.2.: Visualization of vortex beams (in this case Laguerre-Gaussian beams) of different OAM states l. The first two columns show the transversal intensity and phase profile over an x-y plane, while the last column shows the helical structure of a constant phase surface. For $l = 0$, we have the well-known Gaussian beam. For other OAM states, the intensity has a "doughnut" shape, with the radius increasing with $|l|$ and the phase going from 0 to 2π l times per revolution of the azimuthal angle ϕ. A negative value of l reverses the rotation of the phase.

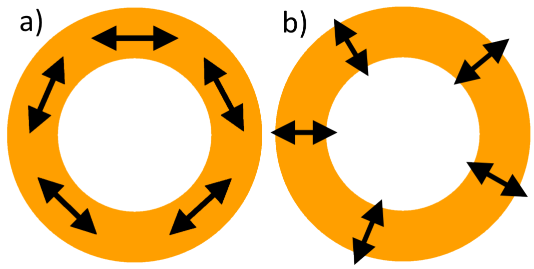

Figure 1.3.: A sketch of the a) azimuthal and b) radial polarizations as seen from a tranversal profile of a vortex beam. They form a basis for vector beams.

OAM in a beam, OAM is surprisingly also an intrinsic property of single photons, each having an OAM of $\pm l\hbar$ [6].

Because polarization describes the light's SAM property, it is entirely independant of OAM. Therefore vortex beams can have any polarization. In particular, vortex beams with a space-varying linear polarization over the tranverse plane are called *vector* vortex beams. Figure 1.3 shows a special pair of orthogonal polarizations for vector beams composed of the radial and azimuthal polarization. Beams with these polarizations are called cylindrical vector beams.

The main examples of beams containing OAM are the Laguerre-Gaussian and Bessel beams. Both are circularly symmetric annular beams, but with different radial distributions of their intensity.

1.2. Applications

The applications of vortex beams are diverse and take advantage of their unique patterns of intensity, phase and polarization. We categorize examples of applications into three main fields: micromanipulation, imaging and communication. The latter is most relevant for the topic of this thesis.

1.2.1. Micromanipulation

The OAM and SAM of light can be transfered into the mechanical OAM and SAM of micro-sized particles [5]. SAM spins a particle on itself while OAM rotates a particle around a point [7–9], making possible the control of a micro-sized machine [10]. If torque can be transfered from light to matter, the reverse is possible too. One can sense a rotating particle and measure its angular velocity by illuminating the particule and measuring the OAM of the reflected light, like an angular version of the Doppler shift [11–14].

A vortex beam can also be used as an optical “tweezer” by trapping particles in its dark core [15,16]. Moreover, this trapping property can be upgraded to a tractor beam. Shzedov *et al.* [17] showed that a specially engineered glass microsphere coated with gold can be trapped in the hole of a vector vortex beam as the heat from the light repulses the sphere. It switches between forward and backward directions by switching the beam polarization from radial to azimuthal, respectively.

1.2.2. Imaging

Vortex beams can increase greatly the resolution in microscopy. The resolution of optical microscopes are fundamentally limited by the diffraction of light. Two spots are discernible only if their separation distance is larger than the Abbe diffraction limit, which is about $\lambda/(2\mathrm{NA})$, where λ is the wavelength of light in vacuum and NA is the numerical aperture of the objective. Clever usage of vortex beams allows us to overcome this limit.

A special technique called stimulated emission depletion (STED) microscopy, which won S. Hell a Nobel Prize in Chemistry in 2014, breaks this limit by making use of the doughnut-shaped intensity of vortex beams [18, 19]. As in conventional fluorescence microscopy, an excitation pulse beam lights up a fluorescent label in a sample and creates excitation spots. However, in STED microscopy, a vortex beam at a lower frequency overlaps the excitation beam to only de-excite the area around the spot while leaving the center untouched. The resulting spot is then the size of the hole of the vortex beam, which is much smaller than the diffraction limit. Willig *et al.* [20] reports a reduction of the spot width by a factor of 3 over conventional confocal microscopy.

One can also tightly focus a radially polarized vortex beam to break the Abbe limit [21]. The best focus would be a time reversed radiation of an atom, or a dipole, and the tight focusing of a radially polarized beam emulates this radiation better than a linearly polarized beam. This tight focus redirects the radial polarization and create a strong longitudinal component at the focus, which has a smaller spot size than the focus spot of a linearly polarized beam. Dorn *et al.* [22] reports a decrease of the spot longitudinal component width by a factor of 1.2 over a linearly polarized beam. The spot shrink factor can be further reduced to 1.4 by blocking the rays closer to the propagation axis with an annular aperture.

The switching laser mode (SLAM) microscopy [23] is similar to STED in that it uses the hole of a vortex beam to shrink the spot size. However, the image is created in two steps in SLAM microscopy: the sample is irradiated with a confocal beam and a vortex beam separately, and then their difference is calculated in post-processing. The best results are with azimuthally polarized vortex beams. Dehez *et al.* [23] reports a decrease of the spot width by a factor of about 2 over conventional confocal microscopy. This method is less precise than STED but is much simpler to perform as there is no need to time two lasers at the same time. It also works for both fluorescent and non-fluorescent environments.

In optical interferometry, one creates a contour map of a sample and measures the height of its features by using the interference between an image carrying wave, reflected on or transmited through a sample, and a reference wave [24]. One problem of this method is that it cannot differentiate maxima from minima. A vortex filter resolves this ambiguity by replacing contour lines by spiral lines, where their orientations switch with elevations and depressions.

Finally, one can perceive a distant planet hidden by the glare of its star using coronagraphy. A vortex phase mask is applied to the telescope which cancels the intensity in the middle while leaving the edges bright [25, 26].

1.2.3. Communication

Since the OAM states are orthogonal to each other, these states can be multiplexed and demultiplexed for communication purposes [27]. Moreover, OAM has in theory an infinite number of orthogonal states which permits the use of high dimensional units of information (compared to, for example, two-dimensional bits with polarization). One can then use a whole alphabet instead of being limited to zeros and ones, which permits more data transmission per pulse. While other spatial bases such as the Hermite-Gaussian modes also provide an infinite basis, the OAM basis is rotationally invariant, a great asset for transmitting OAM through fibre [28].

Finally, the favored application for our proposed device is a cryptographic scheme called quantum key distribution (QKD), which uses the laws of quantum mechanics to detect eavedroppers in a communication channel [2]. While it is possible to use the polarization basis (BB84) [29], the larger basis of OAM provides more degrees of freedom to the algorithm and thus better security [30].

For QKD to work in the BB84 protocol, there needs to be at least two mutually orthogonal bases. With polarization, the two bases can be the vertical/horizontal polarizations and the diagonal/antidiagonal bases. For OAM, one basis can be the pure OAM states and the second basis formed of superpositions of OAM states [2]. We thus need to generate superpositions of vortex beams.

1.3. Vortex beam generation

There already exist multiple ways of generating vortex beams. However, most of them are not scalable and use bulk optics components. In other words, they are relatively large and hard to integrate with other components or need a long propagation path to be integrated. They are convenient in the lab but not for commercial purposes.

The first discovered method was to use cylindrical mode converters to convert Hermite-Gauss modes of a laser cavity into Laguerre-Gauss modes, which can carry OAM [6].

Other methods change the phase front of a laser beam with plates which vary the optical paths over the beam profile through variation of the plate's width or refractive index. A spiral phase plate has a width that varies with azimuthal angle [31–33]. It is relatively cheap but is challenging to fabricate as it requires high precision features. One can also use holograms to generate vortex beams through transmission or reflection [1, 15]. More recently, spatial light modulators have become tools of predilection for beam shaping as they offer a complete dynamic control over a beam phase front. They are great for lab work but are ill-fitted for large scale usage as they are large bulk optics and are very expensive.

There also exist inhomogeneous anisotropic plates called q-plates which convert the SAM to OAM. These plates are made of a birefringent material which optical axis orientation varies over the plate surface. This kind of material have been made with nematic liquid crystal [34] and a plasmonic metasurface [35].

The listed methods all reshape an existing laser beam phase front into a vortex beam by passing it through special lens and thus are not convenient for miniaturization. We choose a different method that uses a device called angular grating, which is a ring resonator with an embedded Bragg grating [3]. The grating is formed of small fragments protruding off either the inner or outer wall of the ring and gives the final structure a gear-like shape, as seen in Fig. 1.4 a). Ideally, we would generate superpositions of vortex beams by stacking vertically many angular gratings of different radii [36]. This multiple level structure is however difficult to fabricate. For our project, we focus instead on creating a modified version of the angular grating on a single level that still generate a superposition of vortex beams. As seen in Fig. 1.4 b), we add a second Bragg grating to the angular grating, such that there is a grating on both the inner and outer walls of a single ring resonator.

Others have also used angular gratings to generate superpositions of vortex beams. Introducing counterpropagating modes in the angular grating leads to a superposition of $\{-l, +l\}$ [37,38]. Another idea is to shape the gratings as sine waves and then combine two or more differents gratings together, resulting in a beating grating pattern [39]. Others have generated superpositions of vortex beams by fabricating a micro-scale spiral phase plate over its own semiconductor laser [33].

Angular gratings have many advantages over the conventional generation methods. The optical components are integrated, which makes the device stable and scalable. The ring is very small with only tens of microns of diameter, the right size to couple to OAM fibres [40]. Furthermore, the material used for the integrated optics, silicon over a silica slab, is complementary metal-oxide-semiconductor (CMOS) compatible, meaning that it can be mixed with integrated eletronic circuits. Finally, the angular grating gets its light directly on the chip, where other optical processing such as modulation and wavelength multiplexing can be carried out. It also means that the angular gratings can work for the reverse process: sorting OAM states [36]. As we will see in chapter 2, a vortex beam with the appropriate OAM state and wavelength can couple in an angular grating and then to a waveguide. For this reason, the idea of a vertical stack of different angular gratings with each its own access waveguide is perfect to unravel the OAM content of a vortex beam.

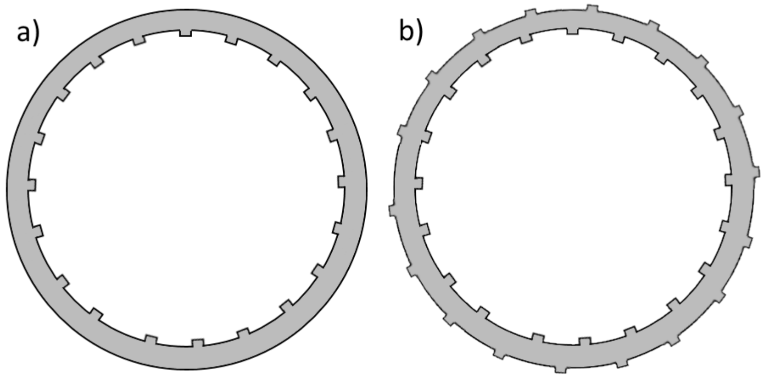

Figure 1.4.: a) An angular grating with a single grating as used in [3] and b) our proposed modified version of the angular grating with two gratings to generate superpositions of vortex beams.

1.4. Conclusion

There are numerous applications for vortex beams, especially in micromanipulation, imaging and communication. There also exists multiple methods of generating vortex beams. The angular grating device is unique among those as it has very small size and is integrated, thus stable and scalable. Generating superpositions of vortex beams using these angular gratings will unlock greater security in communication channels. Now that we understand how OAM works in light and why using angular gratings is advantageous, we will next model analytically how the angular gratings work.

2. Analytical model

This chapter explains how angular gratings generate vortex beams and introduces the theory behind the effects that will be seen in the simulation and experimental results. Our final structure will contain two forms of gratings: a linear grating and an angular grating. The linear grating acts as a coupler between the fibre and the integrated waveguide while the angular grating generates the vortex beam. We will start by explaining how a linear grating works first since it is a simpler structure and it provides a good foundation, then follow with the working of angular gratings. Along the way, we will review the dipole radiation to be able to describe the angular grating scattering with a discrete dipole approximation. We will then extend the model to include angular gratings with two gratings, in order to generate superpositions of vortex beams. We will then address the case of mode splitting that happens, among other causes, when the angular grating has large grating strength. Finally, we will introduce the finite-difference time-domain numerical method, which we will use in the next chapter to get a more accurate picture of the angular grating scattering.

2.1. Grating couplers (Linear gratings)

The first challenge with nanostructures is to induce light into the chip. It is done by focusing the light of an optical fibre into an integrated waveguide, which will then lead the light to the structure of interest. However, this type of coupling is difficult because of the large difference in mode size, with a mode area ratio close to three orders of magnitude.

Our approach to fibre-waveguide coupling is a grating coupler where a grating on waveguide surface couples light in and out [41]. The refractive index of a waveguide is higher than its environment to confine light by total internal reflection. However, a ray entering a waveguide from the side cannot have a suitable angle to be confined. To bend the ray in a direction parallel to the waveguide, we apply a grating on a small portion of the waveguide to use its first-order diffraction. This method gives freedom over the waveguide position on a chip and does not require lensed fibres. A bare fibre end is sufficient so in the instance of a damaged end, one can simply cleave the end without replacing the whole fibre, which cannot be done with lensed fibres.

The high refractive index contrast of a silicon grating induces a high birefringence and renders the grating polarization dependent. We choose to use the TE mode (polarization parallel to the grating grooves) since it has the best polarization for scattering from angular gratings, as we will see in section 2.2.3.

Conservation of momentum, represented schematically in Fig. 2.1, requires that [42]

$$k \sin(\theta_{\text{out}}) = n_{\text{eff}} k \sin(\theta_{\text{in}}) - g\frac{2\pi}{\Lambda}, \tag{2.1}$$

where $k = 2\pi/\lambda$ is the light wavenumber in vacuum, θ_{in} and θ_{out} are the angles of the light inside and outside the waveguide relative to the normal of the chip surface, n_{eff} is the effective refraction index of the mode in the grating, g is an integer representing the diffraction order and Λ is the periodicity of the grating.

The grating periodicity is chosen to maximize the amount of light coupling inside at an angle close to $\theta_{\text{in}} = \pi/2$, parallel to the waveguide to ensure confinement. We also want to limit the number of possible diffraction modes to the first-order ($g = 1$) to maximize power in that mode. By simplicity, we set $\theta_{\text{out}} = 0$ such that the input (or output) fibre is normal to the chip. Then Eq. (2.1) requires $\lambda = \Lambda n_{\text{eff}}$, which is the second-order Bragg wavelength $\lambda_{2\text{B}}$.

Depending on how much θ_{in} can deviate from $\pi/2$ while keeping confinement in the waveguide, a certain bandwidth centred on $\lambda_{2\text{B}}$ will be accepted by the coupler. For example, a 3-dB coupling bandwidth of around 90 nm is reported by Cai *et al.* [41].

The problem with setting $\theta_{\text{out}} = 0$ is that it creates a strong back-reflection of the grating into the waveguide, which can lead to unwanted features such as a Fabry-Perot cavity between the input and output coupling gratings. To avoid this second-order reflection, the fibre is slightly tilted (by about 10° relative to the normal), which blue-shifts the coupling bandwidth [43]. Now that we know how to get light in the access waveguide, we can focus on our desired structure: the angular grating.

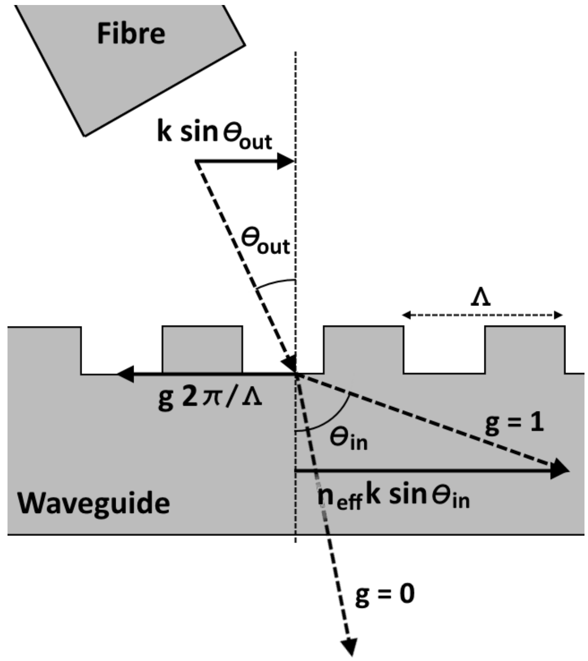

Figure 2.1.: The conservation of momentum for the linear grating coupler in Eq. (2.1). The quantity k is the wavenumber of light in vacuum. Using the first-order diffraction of the grating lets one couple light into the waveguide at $\theta_{\text{in}} > \theta_{\text{out}}$, even though the index inside the waveguide is higher than outside. The figure is not to scale.

2.2. Angular gratings

We begin by describing the optical modes supported in a ring resonator after which we will show how these modes interact with an angular grating.

2.2.1. Ring resonators

An angular grating is essentially a ring resonator with an embedded Bragg grating on the inner or outer wall. Despite this modification, the angular grating retains the basic properties of the ring resonator. As the name suggest, a ring resonator is an on-chip structure where a waveguide is shaped into a ring. A single access waveguide couples light to and from the ring through evanescent waves, as shown in Fig. 2.2. The only wavelengths

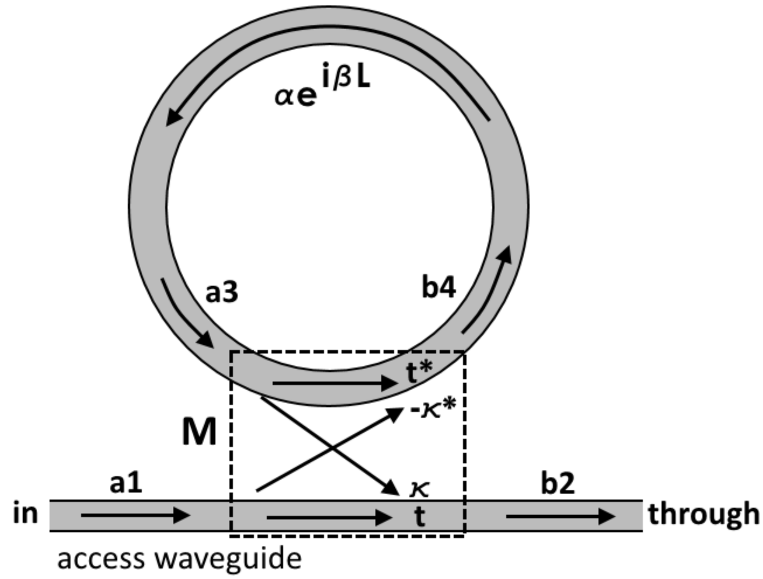

Figure 2.2.: The coupled modes of a ring resonator. The matrix M refers to the coupling region between the access waveguide and the ring, with two incoming modes and two outgoing modes. The quantities t and κ are the transmission and coupling coefficients, respectively. As the mode b_4 transforms into a_3, it gains a factor $\alpha e^{i\beta L}$, where α represents the round trip transmissivity, β is the propagation constant and L is the ring circumference. The figure is not to scale.

coupling to the ring are those that fulfill the resonance condition

$$|p|\lambda = 2\pi R n_{\text{eff}}, \tag{2.2}$$

where p is an integer defining the resonance mode, λ is the wavelength of light in vacuum, R is the radius of the ring and n_{eff} is the effective refraction index for the mode in the ring. In other words, there is resonance if and only if the optical path length in the ring is equal to an integer number of wavelengths. The quantity p is usually positive, as a negative p reverses the propagation direction. All other wavelengths interfere destructively inside the ring and instead pass through the access waveguide without coupling.

A high coupling efficiency between the access waveguide and the ring ensures that an adequate amount of light can enter the resonant mode, but it can also easily couple back to the access waveguide, which reduces the total energy in the resonant mode. To create a

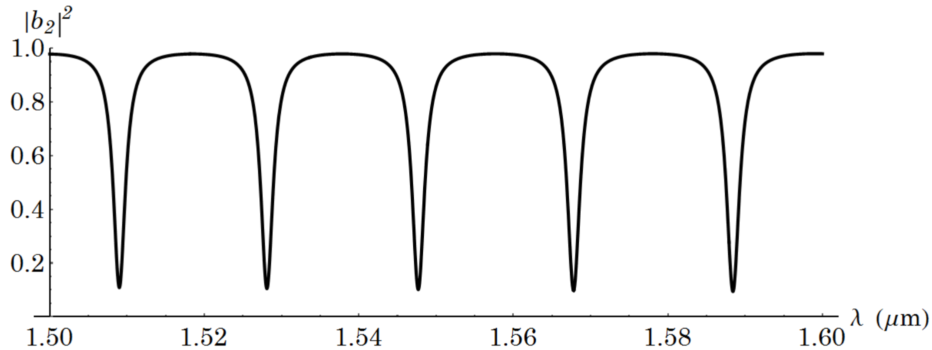

Figure 2.3.: The spectrum of the through port output of the access waveguide (mode b_2) of a ring resonator. The dips are caused by on-resonance wavelengths coupling to the ring. The parameters used for the sketch: $n_{\text{eff}} = 2.4 + i10^{-3}$, $\rho = 0$, $t = 0.9$ and $L = 50.3$.

high quality ring resonator, we must find the optimal coupling coefficient to maximize the energy in the ring [44].

We assume unidirectional modes in the ring, as shown in Fig. 2.2, and a lossless coupling between the access waveguide and the ring. Thus the transfer matrix for the coupling region is

$$\mathrm{M} = \begin{bmatrix} t & \kappa \\ -\kappa^* & t^* \end{bmatrix}, \tag{2.3}$$

where t and κ are the transmission and coupling coefficients, respectively. The * denotes the conjugated complex value. The matrix M is unitary, thus

$$|t|^2 + |\kappa|^2 = 1 \qquad\qquad \kappa t^* + \kappa^* t = 0. \tag{2.4}$$

The ring modes are defined in Fig. 2.2. The relations between these modes are

$$\begin{bmatrix} b_2 \\ b_4 \end{bmatrix} = \mathrm{M} \begin{bmatrix} a_1 \\ a_3 \end{bmatrix}, \qquad\qquad a_3 = \alpha e^{i\beta L} b_4, \tag{2.5}$$

where $\beta = 2\pi n_{\text{eff}}/\lambda$ is the linear propagation constant through the ring and $L = 2\pi R$ is the ring circumference. The quantity α describes the round trip transmissivity, which is limited by the medium absorption and the ring bending loss ($\alpha = 1$ indicates no loss). We then find the amplitude going through the access waveguide and in the ring, respectively designated by b_2 and a_3, in terms of input amplitude a_1:

$$b_2 = \frac{t - \alpha e^{i\beta L}}{1 - \alpha e^{i\beta L} t^*} a_1 \qquad\qquad a_3 = \frac{-\alpha e^{i\beta L} \kappa^*}{1 - \alpha e^{i\beta L} t^*} a_1. \tag{2.6}$$

On resonance, $\beta L = 2\pi p$. The intensity of b_1 and a_3 then become

$$|b_2|^2 = \frac{(|t| - \alpha)^2}{(1 - \alpha|t|)^2} |a_1|^2 \qquad\qquad |a_3|^2 = \frac{\alpha^2(1 - |t|^2)}{(1 - \alpha|t|)^2} |a_1|^2. \tag{2.7}$$

Fig. 2.3 shows a sketch of the transmission spectrum b_2.

Thus for a given α, the intensity in the ring is maximized at critical coupling $|t| = \alpha$, or when the coupling and loss coefficients are equal. In that case, no energy gets through the waveguide ($b_2 = 0$). In a standard ring resonator, one usually wants to maximize the energy confinement in the structure and so to keep α as close to 1 as possible. Since we will scatter light out of the ring to generate beams, there will be more loss on purpose and so we want to reduce α.

A way of assessing the resonator quality of a ring is to measure its quality (Q) factor. The Q factor is related to how long the light remains in the ring and so high Q factor means a high quality ring resonator. In the transmission $|b_2|^2$, a high Q factor translates into narrow resonance dips, while shallow dips indicates losses and so a low Q factor.

Now that we understand the optical mode used as the source for the angular grating, we next consider how to model the individual scattering elements.

2.2.2. Dipole radiation

Here we explain how the light scattered from each element of the angular grating can be modelled by dipole radiation. Combining the contribution of each element will lead to the desired radiation modes.

We make an analytical model of the light scattering from the angular grating based on the work of Zhu *et al.* [45]. The discrete dipole approximation simplify the analysis while keeping good accuracy, as it treats each element of the grating as a dipole with a phase shift to account for the propagation of light through the ring (Fig. 2.4).

We first introduce a general expression for the radiation of a single electric dipole, which is derived in most electrodynamics textbooks for specific cases [46]. One way of deriving the dipole radiation is to start with Jefimenko's equations and use a multipole expansion,

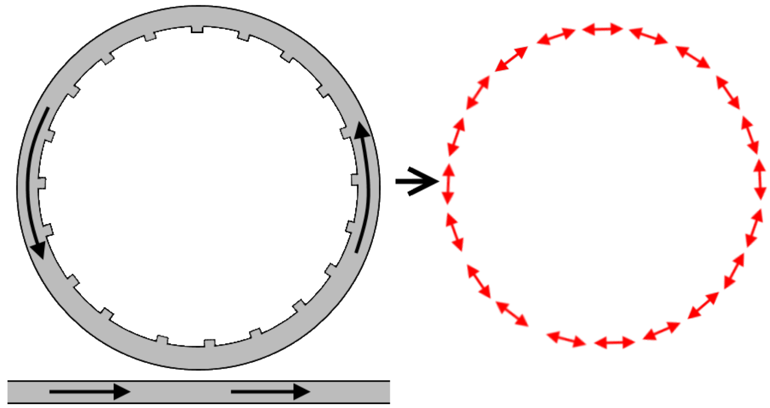

Figure 2.4.: The scattered field of an angular grating can be approximated by replacing each grating element by a dipole.

which is only valid outside the charge distribution [47]. The dipole terms lead the series as there are no point charges (no monopoles). Since light drives the dipole oscillations, we assume the dipole moment to follow an harmonic time dependence $\mathbf{p}(t) = p_o e^{-i\omega t}\hat{\mathbf{p}}$, where p_o and $\hat{\mathbf{p}}$ are the magnitude and unit vector of the dipole moment, respectively. Thus the electric dipole radiation at a distance r is

$$\mathbf{E}(\mathbf{r}) = \frac{p_o}{4\pi\epsilon_o} e^{ikr} \left\{ \frac{k^2}{r} (\hat{\mathbf{r}} \times \hat{\mathbf{p}}) \times \hat{\mathbf{r}} + \left(\frac{1}{r^3} - \frac{ik}{r^2} \right) [3(\hat{\mathbf{r}} \cdot \hat{\mathbf{p}})\hat{\mathbf{r}} - \hat{\mathbf{p}}] \right\}, \tag{2.8}$$

where ϵ_o is the vacuum permittivity and $k = 2\pi/\lambda$ is the light wavenumber in vacuum. The first term (proportional to $1/r$) corresponds to the far field and dominates when $r \gg \lambda$. This is the only term that radiates, meaning that the total power integrated over a sphere is non-zero as r goes to infinity. The other terms correspond to the near field (proportional to $1/r^2$ and $1/r^3$) and dominate when $r \ll \lambda$. In particular, the term proportional to $1/r^3$ stands for the static electric dipole.

2.2.3. Angular grating radiation

As per [45], the angular gratings are made of q dipoles uniformly distributed on a ring of radius R, creating a grating of periodicity $\Lambda = 2\pi R/q$. The total radiated field is then the sum of each dipole radiation.

We assume that the magnitude of each dipole moment is equal, although in reality

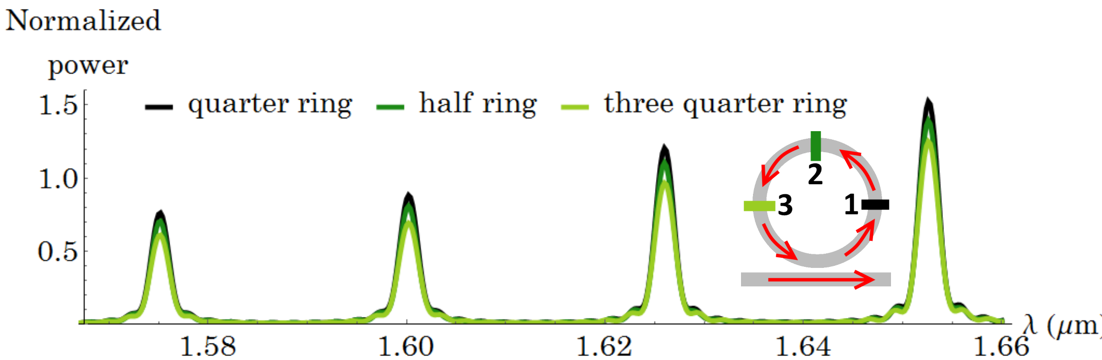

Figure 2.5.: The power spectrum inside an angular grating at one quarter, half and three quarter of the ring (simulated). The power dissipates due to bending loss and the grating scattering.

previous dipole scattering and bending loss lead to a reduction in the energy along the ring as seen in Fig. 2.5.

We also assume the light in the waveguide to be in a transverse electric (TE) mode, which in the integrated optics world means that the polarization is parallel to the slab. This is necessary as a transverse magnetic (TM) mode would create dipoles perpendicular to the slab, which do not scatter well in the out-of-plane direction.

While most of the TE single mode energy is in the polarization transversal to the waveguide, a small, often neglected, part of the energy is in the polarization longitudinal to the waveguide. The transversal and longitudinal polarizations of the waveguide then become the radial and azimuthal polarizations of the ring, respectively. Figure 2.6 shows that these polarizations are in different spatial modes, where the radial polarization is centred in the waveguide and the azimuthal polarization sticks to the lateral walls. Since the scatterers are placed on the lateral walls of a ring, the azimuthal component of the ring mode drives the dipole moments in the azimuthal direction ($\hat{\mathbf{p}} = \hat{\boldsymbol{\phi}}$). If the scatterers were in the middle of the waveguide, the dipole moments would be in the radial direction [48].

The last step is to determine the phase shift due to propagation through the ring between each dipole. If we consider only a small section of the ring at a time, we can approximate the waveguide to be straight. In that case, we can reuse the phase matching condition of

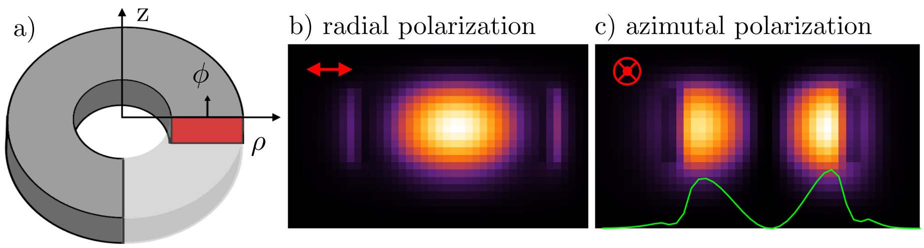

Figure 2.6.: Simulation of the E-field intensity profile of a portion of the ring, located in red in a), for the b) radial and c) azimuthal polarizations. The red arrows show the polarization on that plane. The radial component is 20 times brighter than the azimuthal component. The spatial modes for the radial and azimuthal polarizations lie in the centre and on the lateral walls of the waveguide, respectively. The green curve in c) is a cross section plot of the the transversal plane to help to see that the intensity is slightly higher on the outer wall. The pixelation is an artifact of the simulation meshing.

a linear grating in Eq. (2.1):

$$\beta_{\text{rad}} = \beta_{\text{RRM}} - g\frac{2\pi}{\Lambda}, \tag{2.9}$$

where β_{rad} and β_{RRM} are the propagation constants for the radiating wave over the ring and the mode inside the ring resonator, respectively. Both of these propagation constants are defined parallel to the slab. As in section 2.1, g is the diffraction order and Λ is the periodicity of the grating.

If we assume light to go in direction ϕ, starting at $\phi = 0$, it is convenient to instead use the angular propagation constant $\nu = \beta R$. This means that for a circular arc length s, the propagation phase becomes $\beta s = \beta R\phi = \nu\phi$. Then Eq. (2.9) transforms into:

$$\nu_{\text{rad}} = \nu_{\text{RRM}} - gq, \tag{2.10}$$

where $\nu_{\text{rad}} = \beta_{\text{rad}} R$ and $\nu_{\text{RRM}} = \beta_{\text{RRM}} R$ are the angular propagation constants for the radiating wave over the ring and the ring resonator mode, respectively, and $q = 2\pi R/\Lambda$ is the number of grating elements. Equation 2.10 can also be derived through coupled mode theory, where the ring resonator modes are perturbed by the grating [3]. Since the radiated field has a dependency on the azimuthal angle of $e^{i\nu_{\text{rad}}\phi}$, then ν_{rad} takes on the role of the radiated OAM order. Consequently, we rename $\nu_{\text{rad}} \equiv l$. Moreover, $\nu_{\text{RRM}} = 2\pi R n_{\text{eff}}/\lambda$ is simply the ring mode number p. We can then rewrite Eq. (2.10) as

$$l = p - gq. \tag{2.11}$$

The quantities p, g and q are all integers and so is l. Since β_{rad} is one of the components of the wave vector $\mathbf{k}_{\text{rad}} = \beta_{\text{rad}}\hat{\boldsymbol{\phi}} + k_\rho\hat{\boldsymbol{\rho}} + k_z\hat{\mathbf{z}}$, the magnitude of the angular propagation constant is bounded by

$$|\nu_{\text{rad}}| < |k_{\text{rad}}R| = \left|\frac{2\pi R}{\lambda}\right|, \tag{2.12}$$

which means

$$|l| = |p - gq| < \left|\frac{2\pi R}{\lambda}\right|. \tag{2.13}$$

These bounds define the forbidden areas of l, as seen in Fig. 2.7. We can also find from Eq. (2.13) the possible values of g:

$$\frac{2\pi R}{\lambda q}(n_{\text{eff}} - 1) < g < \frac{2\pi R}{\lambda q}(n_{\text{eff}} + 1) \tag{2.14}$$

where it is clear that $g > 0$ when $p > 0$.

The phase acquired up to the m-th element by propagation through the ring alone is thus $l\phi_m$, where ϕ_m is the azimuthal angle of the m-th dipole. The m-th dipole moment becomes

$$\mathbf{p}_m(t) = p_o e^{-i\omega t} e^{il\phi_m}\hat{\boldsymbol{\phi}}_m. \tag{2.15}$$

We now set cylindrical coordinates with the origin in the centre of the ring, as seen in Fig. 2.8. By inserting Eq. (2.15) in the far field part of Eq. (2.8) and summing over all q dipoles, the electric radiation of the angular grating at some point $P = (\rho, \phi, z)$ is

$$\mathbf{E}(\rho, \phi, z) = \frac{p_o k^2}{4\pi\epsilon_o}\sum_{m=1}^{q} e^{ikr_m} e^{il\phi_m}\left[\frac{1}{r_m}\hat{\boldsymbol{\phi}}_m + \frac{\rho\sin(\phi_m - \phi)}{r_m^2}\hat{\mathbf{r}}_m\right], \tag{2.16}$$

where $\mathbf{r}_m$ is a vector going from the m-th dipole to the point P and has a magnitude $r_m = \sqrt{z^2 + \rho^2 + R^2 - 2\rho R\cos(\phi_m - \phi)}$.

At this point, we have found the scattered electric field above an angular grating. However, it does not give much insight into what the intensity or the phase look like unless we calculate it numerically. Even in that case, the high number of terms, with each term containing a rather large equation, makes the calculation time-consuming. We thus simplify Eq. (2.16) with reasonable approximations. We set $\rho \ll z$ since any light too far from the

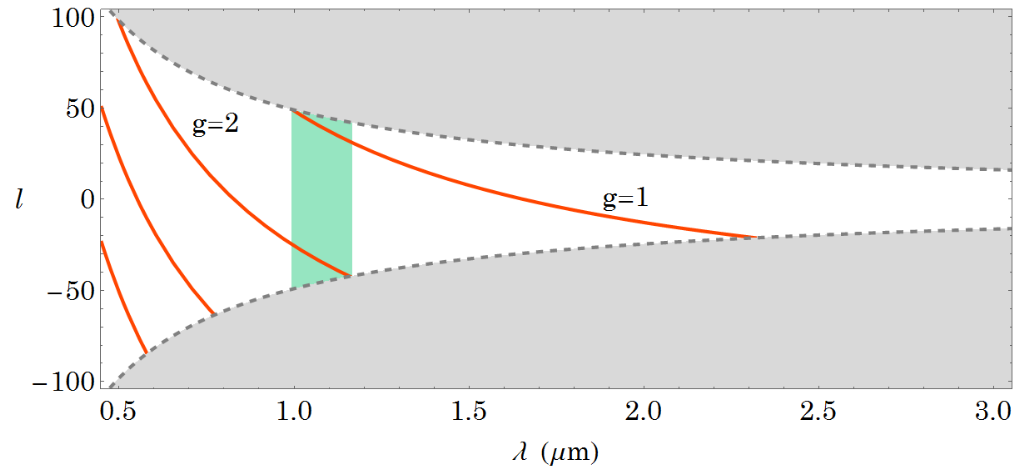

Figure 2.7.: The possible OAM states l over λ for different values of diffraction order g as given by Eq. (2.13). The grey areas are forbidden. Some ranges of wavelength allow more than one order of diffraction at the same time, such as the section in green. The number of simultaneous orders of diffraction increases as the wavelength shortens. The parameters used for this plot are those of our ultimate angular grating, which are: $R = 7.8$ µm, $q = 74$ and $n_{\text{eff}} = 2.5$. We work at $\lambda \approx 1.5$ µm and so $g = 1$.

propagation axis will not be detected by our sensor. Thus the polarization of Eq. (2.16) becomes completely azimuthal[1]:

$$\mathbf{E}(\rho, \phi, z) = \frac{p_o k^2}{4\pi\epsilon_o} \sum_{m=1}^{q} \frac{e^{ikr_m}}{r_m} e^{il\phi_m} \hat{\boldsymbol{\phi}}_m. \tag{2.17}$$

We then Taylor expand the square root of r_m with $R^2 \ll z^2 + \rho^2$. The phase is much more sensitive than amplitude to errors due to its 2π-periodicity. Therefore, we use a first order approximation for the phase and the zeroth order approximation for the amplitude:

$$\mathbf{E}(\rho, \phi, z) = \frac{p_o k^2}{4\pi\epsilon_o} \frac{e^{ikr}}{r} \sum_{m=1}^{q} e^{-ik_\rho R \cos(\phi_m - \phi)} e^{il\phi_m} \hat{\boldsymbol{\phi}}_m, \tag{2.18}$$

where $r = \sqrt{z^2 + \rho^2}$ is the spherical radius with the origin in the middle of the ring and $k_\rho = k\rho/r$ is the radial component (in cylindrical coordinates) of the wavenumber.

[1] Even in the case of $\rho > z$ (such as $\rho = 1$, $z = 0$ for example), the second term of Eq. (2.16) is still negligible.

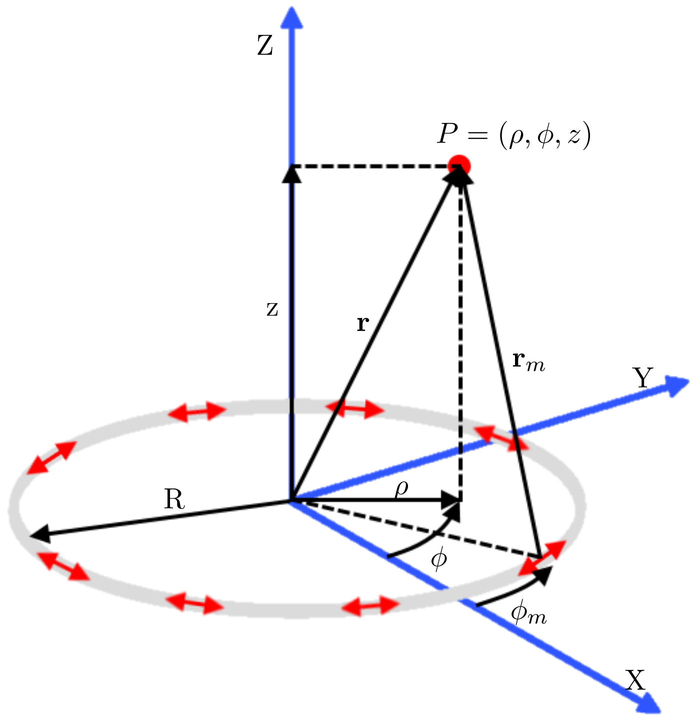

Figure 2.8.: The coordinate system for the dipole approximation method. The red arrows are azimuthally polarized dipoles, each placed at a radius R, angle ϕ_m and $z = 0$. The electric field is calculated at a point P. The generated vortex propagates along the z-axis.

Furthermore, when $q \gg 2\pi$ the discrete sum approaches an integral

$$\begin{aligned}\sum_{m=1}^{q} e^{-ik_\rho R\cos(\phi_m-\phi)}e^{il(\phi_m-\phi)} &\approx \frac{q}{2\pi}\int_0^{2\pi} e^{-ik_\rho R\cos(\phi_m-\phi)}e^{il(\phi_m-\phi)}\,d\phi_m \\ &= qi^{-l}J_l(k_\rho R)\end{aligned} \tag{2.19}$$

where we introduce the Bessel function of first kind

$$J_n(x) = \frac{1}{2\pi i^n}\int_0^{2\pi} e^{ix\cos(\tau)+in\tau}\,d\tau. \tag{2.20}$$

The final expression of the field depends on the choice of polarization basis. Due to the cylindrical symmetry of the field, a natural basis for the transversal polarization is the

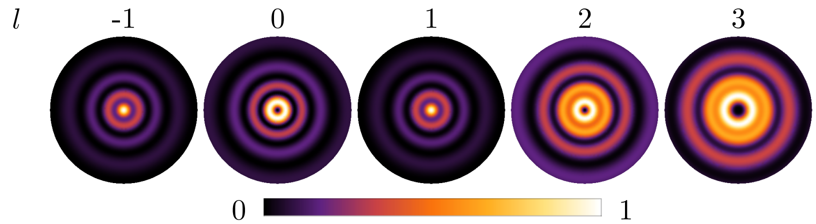

Figure 2.9.: The total intensity radiated from an angular grating in the far field ($z = 1$ m) for different OAM l states. Note that the $l = 0$ state has a zero intensity centre while the $l = \pm 1$ states have non-zero intensity centres, an effect only possible with vector beams.

radial and azimuthal polarizations:

$$\mathbf{E}(\rho, \phi, z) = \frac{qp_o}{4\pi\epsilon_o} k^2 \frac{e^{ikr}}{r} i^{-l} e^{il\phi} \left(\frac{l}{k_\rho R} J_l(k_\rho R) \hat{\boldsymbol{\rho}} + i J_l'(k_\rho R) \hat{\boldsymbol{\phi}} \right), \tag{2.21}$$

where $J_l'(x) = dJ_l(x)/dx$. Both polarizations have an OAM state l. On the other hand, the circular polarization basis $\hat{\mathbf{L}}$ and $\hat{\mathbf{R}}$ offers a more insightful form:

$$\mathbf{E}(\rho, \phi, z) = \frac{qp_o}{4\pi\epsilon_o} k^2 \frac{e^{ikr}}{r} \frac{i^{-l}}{\sqrt{2}} \left(e^{i(l-1)\phi} J_{l-1}(k_\rho R) \hat{\mathbf{L}} + e^{i(l+1)\phi} J_{l+1}(k_\rho R) \hat{\mathbf{R}} \right). \tag{2.22}$$

Here the left and right circular polarizations have OAM states $l_\mathrm{L} = l - 1$ and $l_\mathrm{R} = l + 1$, respectively. Thus the OAM state is polarization dependent. The Eq. (2.22) tells us that the far-field radiation of an angular grating is essentially a spherical wavefront with a twist in the centre and has an amplitude radial distribution modulated by a Bessel function.

We see in Fig. 2.9 the intensity profile of the radiated vortex beams. The $l = 0$ state is doughnut-shaped while the $l = \pm 1$ states have non-zero intensity centres, which is the opposite of what we would expect of OAM beams. The reason is that we usually work with uniformly polarized beams, but in this case we have vector beams.

We have thus modelled the radiated field of an angular grating by the dipole approximation and confirmed that it will radiate OAM-carrying light perpendicularly to the slab.

2.2.4. Double grating

Having established how an angular grating can generate fields with OAM, we next explore how to generate superpositions of these OAM beams. We add a second grating such that

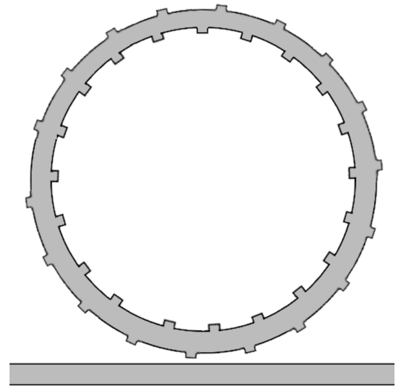

Figure 2.10.: Sketch of an angular grating with two gratings.

there are gratings on both the lateral inner and outer walls of a single ring resonator, as depicted in Fig. 2.10. We have to take into account the relative rotation of the two gratings as their respective radiations will interfere. We thus define the azimuthal position of the m-th dipole for the j-th (1 or 2) grating

$$\phi_{j,m} = \frac{2\pi m}{q_j} + \phi_{j,o}, \tag{2.23}$$

where $\phi_{j,o}$ is the azimuthal position of the zeroth element ($m = 0$) of the j-th grating. One can derive that the phase due to propagation alone at angle $\phi_{j,m}$ is $p\phi_{j,m} = l_j\phi_{j,m} + g_j q_j \phi_{j,o}$. The m-th dipole moment of the j-th grating is therefore

$$\mathbf{p}_{j,m}(t) = p_{o,j} e^{-i\omega t} e^{il_j\phi_{j,m}} e^{ig_j q_j \phi_{j,o}} \hat{\boldsymbol{\phi}}_{j,m}, \tag{2.24}$$

For a given grating, $\phi_o < 2\pi/q$ as the grating returns to its initial position at this point.

Then, following the same steps as in section 2.2.3, the total field radiation for two gratings is simply the superposition of the individual gratings radiation (plus a phase factor accounting for the gratings relative rotation):

$$\mathbf{E}(\rho, \phi, z) = \mathbf{E}_{l_1}(\rho, \phi, z) e^{ig_1 q_1 \phi_{1,o}} + \mathbf{E}_{l_2}(\rho, \phi, z) e^{ig_2 q_2 \phi_{2,o}}, \tag{2.25}$$

where $\mathbf{E}_{l_j}$ can be either Eq. (2.21) or Eq. (2.22) with OAM state l_j. We redefine them as

$$\mathbf{E}_l(\rho, \phi, z) = \mathbf{A}_l(\rho, \phi, z) i^{-l} e^{il\phi}, \tag{2.26}$$

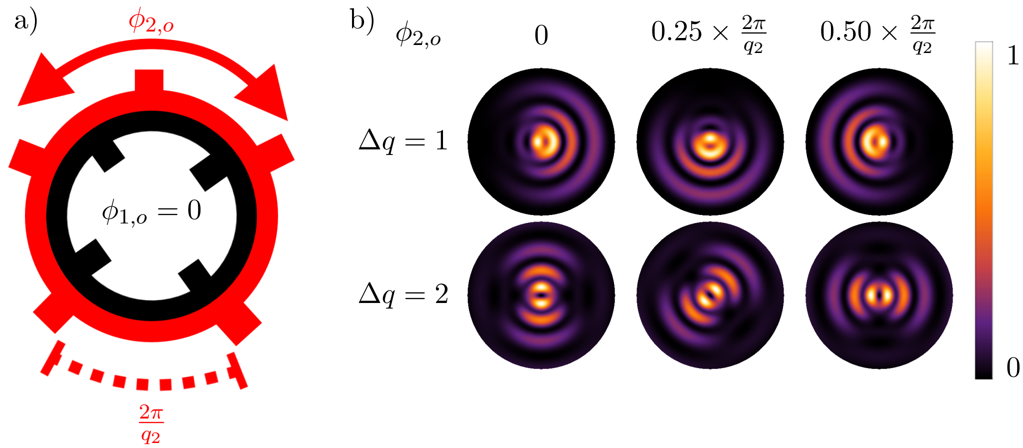

Figure 2.11.: The effect of the gratings rotation on the radiation profile. a) A sketch of an angular grating with $\Delta q = 1$. The outer grating (red) is rotated by $\phi_{2,o}$, while the inner grating (black) is kept constant at $\phi_{1,o} = 0$. The outer grating goes back to its initial position after a rotation of $2\pi/q_2$. b) The radiation pattern as a function of $\phi_{2,o}$, for the cases of $\Delta q = 1$ and $\Delta q = 2$ (we set $g = 1$). For a given grating rotation, the $\Delta q = 1$ pattern rotates twice as far as the $\Delta q = 2$ pattern.

where $\mathbf{A}_l(\rho, \phi, z)$ can be in any basis. A careful choice of basis removes the ϕ dependence on $\mathbf{A}_l$, but for any basis the intensity $|\mathbf{A}_{l_1}|^2$ and the dot product $\mathbf{A}_{l_1} \cdot \mathbf{A}_{l_2}$ lose the ϕ dependence for all l_1 and l_2. This means that the intensity of Eq. (2.25) is[2]

$$|\mathbf{E}(\rho, \phi, z)|^2 = |\mathbf{A}_{l_1}|^2 + |\mathbf{A}_{l_2}|^2 + 2(\mathbf{A}_{l_1} \cdot \mathbf{A}_{l_2}) \cos\left(\Delta l(\phi - \pi/2) + \Delta(gq\phi_o)\right), \tag{2.27}$$

where only the argument of the cosine is dependent on ϕ. Thus the number of bright (or dark) spots on a given radiation ring is Δl and, for given values of $\phi_{o,1}$ and $\phi_{o,2}$, the pattern shifts by $\Delta(gq\phi_o)/\Delta(gq)$ radians, as shown in Fig. 2.11.

2.2.5. Mode splitting

Up until now we focused on ring resonators and angular gratings with unidirectional modes. However, the presence of reflection in the ring leads to coupled contra-propagating modes. These modes are non-degenerate [49] and thus create what we call mode splittings, as seen in Fig. 2.12.

[2] While the amplitude of $\mathbf{A}_l$ differs for each grating, its phase term remain constant and thus $\mathbf{A}_{l_1} \cdot \mathbf{A}_{l_2}$ is real-valued.

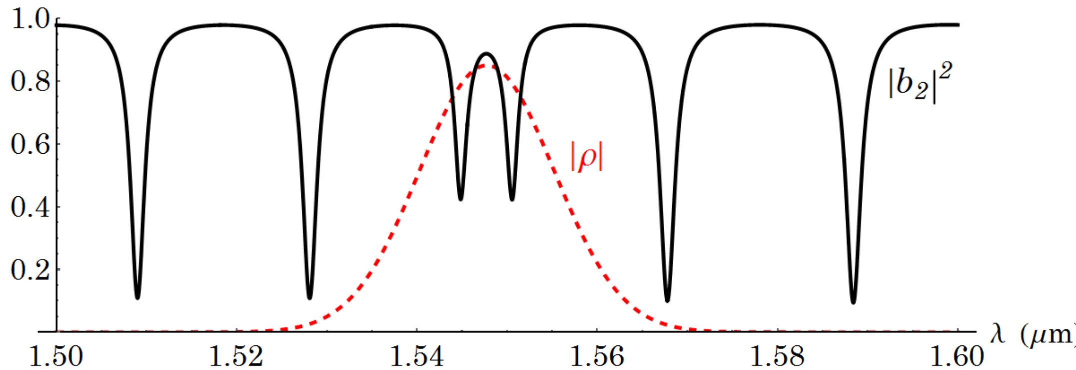

Figure 2.12.: The spectrum of the through port output of the access waveguide (mode b_2) of a ring resonator (solid black line) as in Fig. 2.3, but with a wavelength dependent reflection coefficient (dashed red line). A resonance dip splits into two smaller dips where the reflection is highest.

In standard ring resonators, a reflection can be created by the coupling region but it is usually very low. Angular gratings, however, can act as second-order Bragg gratings, similarly to the grating couplers in section 2.1. For a strong grating (e.g. large elements size), this creates a strong reflection centred on the resonance where $l = p - gq = 0$ since

$$\lambda = \frac{2\pi R n_{\text{eff}}}{p} = \frac{2\pi R n_{\text{eff}}}{gq} = \frac{n_{\text{eff}}\Lambda}{g}, \tag{2.28}$$

which is the $2g$-order Bragg wavelength. Thus the angular grating reflects light for a bandwidth centred on the $l = 0$ wavelength, which splits the $l = 0$ resonance [50]. Other resonances nearby may also be split if the reflection bandwidth is large enough [51].

We derive here how reflection in the ring causes a mode splitting [52]. For the grating, we define the scattering matrix

$$\mathrm{S} = \begin{bmatrix} \rho & \tau \\ \tau^* & -\rho^* \end{bmatrix}, \tag{2.29}$$

where τ and ρ are the transmission and reflection coefficients, respectively. Note that Eq. (2.29) is independent of where on the ring the reflection happens.

The transfer matrix for the coupling region between the access waveguide and the ring

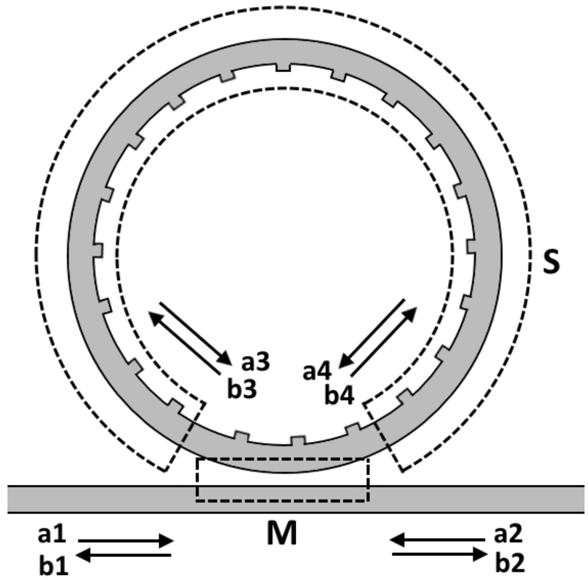

Figure 2.13.: The coupled modes of a ring resonator with a Bragg grating. The matrix M refers to the coupling region between the access waveguide and the ring, and S refers to the grating region which reflects light. The figure is not to scale.

is the same as for a standard ring resonator in Eq. (2.3):

$$\mathrm{M} = \begin{bmatrix} t & \kappa \\ -\kappa^* & t^* \end{bmatrix}, \tag{2.30}$$

where t and κ are the transmission and coupling coefficients, respectively. We assumed no loss at the coupling region or at points of reflection by ensuring that the matrices S and M are unitary:

$$|\tau|^2 + |\rho|^2 = 1 \qquad\qquad \rho\tau^* + \rho^*\tau = 0 \tag{2.31}$$

$$|t|^2 + |\kappa|^2 = 1 \qquad\qquad \kappa t^* + \kappa^* t = 0 \tag{2.32}$$

Fig. 2.13 defines the modes amplitude and their direction in the angular grating. Contrary to section 2.2.1 with a standard ring resonator, here we consider contra-propagating modes. The relations between the modes are thus

$$\begin{bmatrix} b_2 \\ b_4 \end{bmatrix} = \mathrm{M} \begin{bmatrix} a_1 \\ a_3 \end{bmatrix}, \qquad \begin{bmatrix} b_1 \\ b_3 \end{bmatrix} = \mathrm{M} \begin{bmatrix} a_2 \\ a_4 \end{bmatrix}, \qquad \begin{bmatrix} a_3 \\ a_4 \end{bmatrix} = \alpha e^{i\beta L} \mathrm{S} \begin{bmatrix} b_3 \\ b_4 \end{bmatrix}, \tag{2.33}$$

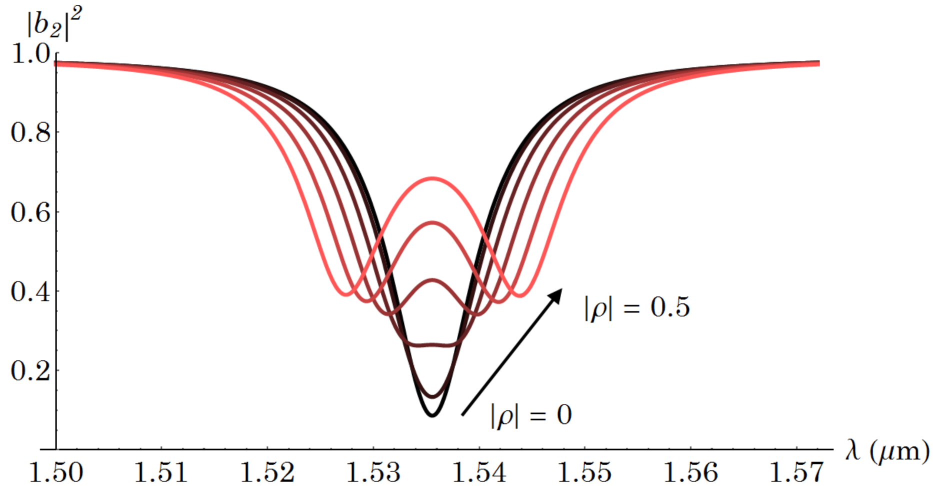

Figure 2.14.: Focus on one resonance of the access waveguide output mode b_2 for different values of the reflection coefficient ρ in the ring resonator as per Eq. (2.34). As ρ increases, the dip splits further apart and becomes shallower.

where in the latter equation we add a propagation phase shift. The quantity $L = 2\pi R$ is the ring circumference and $\beta = \omega n_{\text{eff}}/c$ is the linear propagation constant through the ring, where ω is the angular frequency, n_{eff} is the effective refraction index of the mode in the angular grating and c is the speed of light. The quantity α is still the round trip transmissivity and is reduced by the absorption of the medium and the ring bending loss but also the scattering out of the ring which we want to maximize. We set $a_2 = 0$ to excite the access waveguide from only one side at a time. The resulting amplitude for the output mode of the access waveguide is [52]

$$b_2 = \frac{1}{2}\left(\frac{t - \alpha e^{i\beta L}(\tau + \rho)}{1 - \alpha e^{i\beta L} t(\tau + \rho)} + \frac{t - \alpha e^{i\beta L}(\tau + \rho^*)}{1 - \alpha e^{i\beta L} t(\tau + \rho^*)}\right) a_1. \tag{2.34}$$

The first term is the result of setting $a_1 = a_2$ while the second term is the result of $a_1 = -a_2$, and so they are named symmetric and antisymmetric excitation, respectively. The resonance mode at the complex frequency ω_o occurs at the pole of each term. The imaginary part of ω describes the damping of the ring cavity resonance. Figure 2.14 shows how the mode splitting increases with reflection coefficient ρ. Notice that the dips gets shallower as the energy is split between the two modes. Without reflection ($\rho = 0$, $\tau = 1$), the amplitude goes back to the case of a standard ring resonator as in Eq. (2.6).

If we add a second grating to the ring, a mode splitting will happen as long as the grating causes a high reflection. In the case of a straight waveguide with different gratings on each side, the resulting reflection spectrum is essentially the superposition of the spectra of the individual gratings [53]. By analogy, we can assume that the curved version of this double grating waveguide will produce two reflection bandwidths, each centred on the $l = 0$ resonance of their respective gratings. Thus any resonance generating a superposition state containing the $l = 0$ state has a chance of splitting, depending on the strength of the grating.

2.3. Numerical method

Up to now, we have used the dipole approximation, which is a good method to easily get the generated field. However, it doesn't account for some physical dimensions such as the ring resonator dimensions, the gap length between the access waveguide and the ring affecting coupling, or how the grating elements size and shape change the scattering efficiency. We must optimize those details before designing the real structure. For a more in-depth analysis, we use the finite-difference time-domain (FDTD) method with Lumerical [54], a popular software for designing nanostructures.

The FDTD method uses a 3D model of the structure where we specify the mode and location of a light pulse at a time $t = 0$. A mesh then discretizes the entire simulation space into small volumes to describe the evolution in time of the electromagnetic fields at every point in that space. A finer mesh gives more accurate results but is time consuming. On the other hand, a coarse mesh is faster to simulate but with the trade-off of more rough, potentially wrong, results. At each increment of time step, the light fields are calculated using Maxwell's equations. At the end of the simulation, we have the fields at any point in the 3D space in the time domain. A Fourier transform provides the frequency domain of the fields. For a more detailed description, see [55]. This method is very powerful as it can tackle complex structure geometries. However, its main drawback is its large time-consumption and its need for large amount of memory. In our case, we used a cluster of 40 Gb of memory and each simulation took around five hours.

Since the computation time scales linearly with volume, the far-field is practically impossible to simulate directly with FDTD. Instead, we extrapolate far-field results from the near-field data calculated by FDTD on a surface called a monitor just above the ring. We assume that the remaining part of the space domain is homogeneous and that the field is completely contained by the monitor for that plane (the outside is zero). We can then decompose the near-field data into a plane wave basis and propagate them to the required distance. With Lumerical, the waves are propagated onto a hemispherical surface of 1 m radius, and then projected on a plane for visualization. By simulating the fields interacting with the physical device, the FDTD method allows us to determine the key feature sizes, such as the waveguide width, the grating elements size and the access waveguide to ring resonator coupling gap, necessary to design and fabricate an actual device.

2.4. Conclusion

We have seen how light is coupled from a fibre to an integrated waveguide with a linear grating, then coupled to a ring resonator that accepts only specific wavelengths, and finally transformed into a vortex beam using an angular grating. A superposition of vortex beams is generated if two gratings are applied on a same single ring. We have also seen that a resonance splits into smaller resonances if there are significant reflections in the ring. We used a discrete dipole approximation to predict the radiation patterns of these devices in the far-field and introduced the FDTD method to assess the effect of the physical dimensions on the radiation. The next chapter will compare the results from approximations with more in-depth simulations using the FDTD method.

3. Simulations

In this chapter, we will optimize the parameters of the angular grating to maximize the generated vortex beam intensity. We will look at how the size of the grating's elements affects the intensity of the scattering and compare the effectiveness of using dents or teeth as such elements. We will then proceed to verify the analytical results derived in chapter 2, first for a single grating and then for double gratings. To do so, we will use the finite-difference time-domain (FDTD) method as described in section 2.3.

The simulated angular gratings will all share some parameters. The ring resonators will have a small radius (3.9 μm) to minimize the computation time. This is the same radius as one of the angular gratings for the experimental demonstration of Cai *et al.* [3]. However, a larger radius would improve the access waveguide-ring coupling (as it extends the coupling length) [56] and decrease the bending loss (as it relaxes the curvature). The waveguides will be made of silicon (Si) on a silica glass (SiO_2) substrate. The simulation will start with a pulse of light of power P_o already in the access waveguide, so we do not take into consideration the fibre to waveguide coupling (section 2.1). The waveguides will have a width of 500 nm and a height of 200 nm to support a single TE mode (parallel to the chip slab) around $\lambda = 1550$ nm. The other parameters will be optimized in the next section.

3.1. Angular gratings parameters fine tuning

We must select the parameters of the angular grating to maximize its upward scattering. First, if more light couples from the access waveguide to the ring, more light can scatter out. The coupling coefficient increases as the gap between the waveguide and the ring shortens but, as we have seen in section 2.2.1, the highest energy in the ring occurs at critical coupling, where the coupling coefficient is equal to the loss in the ring. Figure 3.1 shows the power scattered above an angular grating (with number of grating elements $q = 36$) as a function of the gap size, from FDTD. This power is defined as the peak power

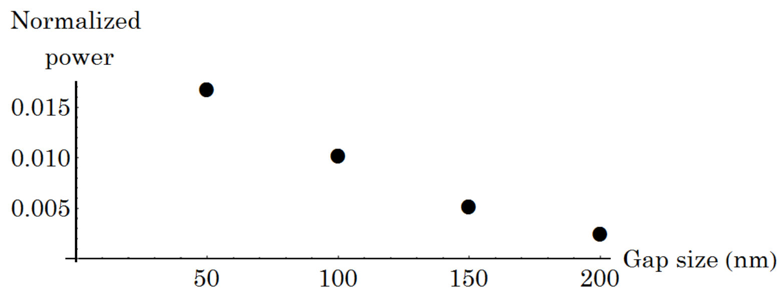

Figure 3.1.: The power scattered above an angular grating ($q = 36$) as a function of the gap size between the access waveguide and the ring. This power is defined from FDTD as the peak power of the $l = 0$ resonance, normalized to integrated power P_o. The power increases with smaller gaps.

of the $l = 0$ resonance, and is integrated over a hemispherical surface in the far-field. In this thesis, the scattered power is always normalized to the integrated power P_o, which is the starting power in the waveguide. We see that the power increases as the gap shortens, or as the coupling efficiency increases. It is not the effect expected from standard ring resonators, where critical coupling occurs at a precise gap size. Angular gratings have a higher loss than ring resonators (because of the intentional large scattering) and so we want a large coupling coefficient. Thus we want the shortest gap possible, while leaving enough space for grating elements on the outer wall of the ring.

Next are the degrees of freedom of the grating elements. We focus on 1) adjusting the elements' size, 2) checking whether an inner or outer grating scatters better, and 3) comparing "teeth" elements, where material protrudes from the ring, to "dents", where holes dig into the ring. We also check whether the same grating elements will work differently for the inner and outer gratings. For simplicity, we take square-shaped elements. We could look at different shapes but the elements are so small that any finer details are lost during fabrication. We also dismiss elements of different materials as it would make the fabrication more difficult.

Figures 3.2 to 3.4 show how these elements' parameters affect the scattering power as a function of wavelength for teeth and dents grating elements, respectively. We start with elements of side 60 nm (as used by Cai *et al.* [3]) and go up to 150 nm, the limit for the outer teeth elements before they overlap the access waveguide for our chosen gap size.

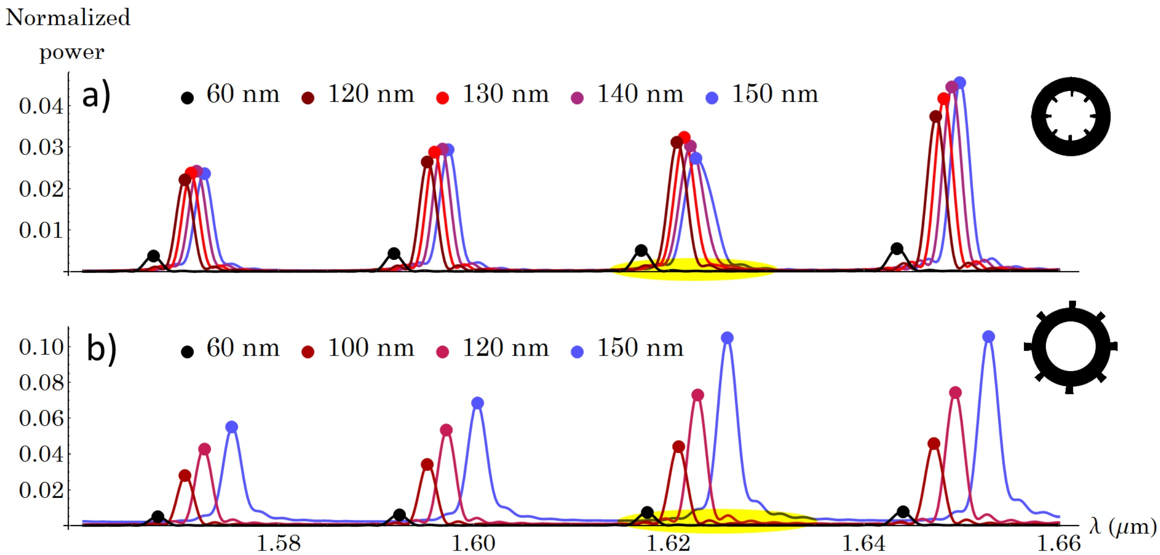

Figure 3.2.: The power spectrum scattered above the angular grating, normalized to integrated power P_o, for angular gratings with teeth elements of different sizes. There are a) inner wall and b) outer wall gratings. The yellow marks highlight the $l = 0$ resonance peaks. The outer grating scattering power is higher that the inner grating. The resonance peaks shift with the elements size as it modifies the effective index. Moreover, for a given element size, the power increases with wavelength because the coupling between the access waveguide and the ring is wavelength dependent. The power increases with the size of the elements except for the $l = 0$ peaks of the inner grating. A magnified view of this region of the spectrum is provided in Fig. 3.3.

Each peak happens at a resonance mode of the ring and has a different orbital angular momentum (OAM) state l. The $l = 0$ resonance peaks are highlighted with a yellow mark.

For Fig. 3.2 (teeth elements), the peaks position shifts with the elements size due to the change in effective index of the mode in the ring. For a given element size, the peak power grows with wavelength because the access waveguide-ring coupling is wavelength dependent. Moreover, the outer wall teeth in b) radiate more than the inner wall teeth in a), as the ring mode centre lies closer to the outer wall. We also see that the larger elements scatter more power, except for $l = 0$ in a). Figure 3.3 shows a magnified view of this region of the spectrum. We see that the maximum power occurs for elements of size

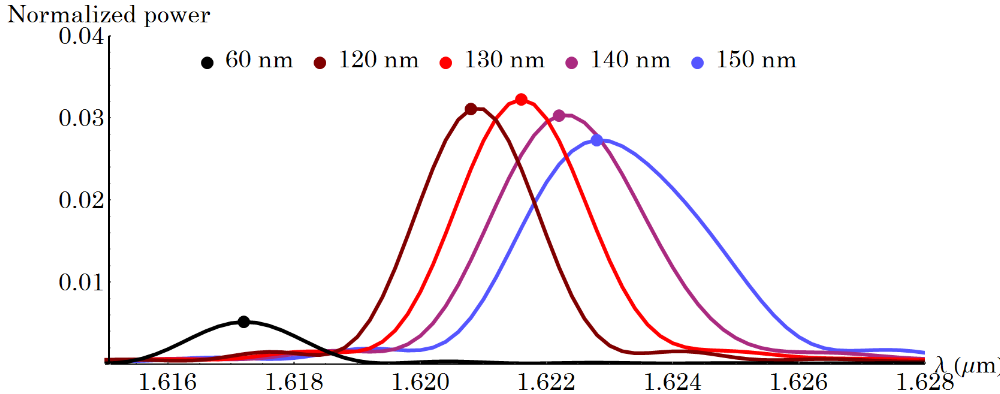

Figure 3.3.: The magnified view of the $l = 0$ resonance (highlighted in yellow) of the inner teeth grating scattering power from Fig. 3.2 a). The maximum power occurs for elements side of 130 nm. Larger elements then decrease the power, likely due to a mode splitting as can be seen from the asymmetry of the peak for size of 150 nm.

130 nm. At 150 nm, the mode starts to splits, as seen from the slightly asymmetric peak, and causes a power decrease (see section 2.2.5).

For Fig. 3.4 (dents elements), the effect is much more chaotic. There are clear mode splittings on the $l = 0$ resonance peaks already at element size 60 nm and the splittings grow with the elements' size. At 150 nm, the overall spectrum power is reduced, likely caused by the dents elements interfering with the ring mode. The scattered power of dents elements is also much smaller than for teeth elements, with at best half of the power of inner teeth or a fifth of the power of outer teeth elements.

To summarize, the maximum power for the generated vortex occurs for these optimal parameters: 1) smallest gap possible between access waveguide and ring, 2) teeth elements instead of dents elements and 3) biggest elements possible (before creating mode splittings). The outer wall grating also radiates with more power than an inner wall grating. As a result, we dismiss dents elements for subsequent simulation, and compromise between the gap and elements sizes so that they do not overlap.

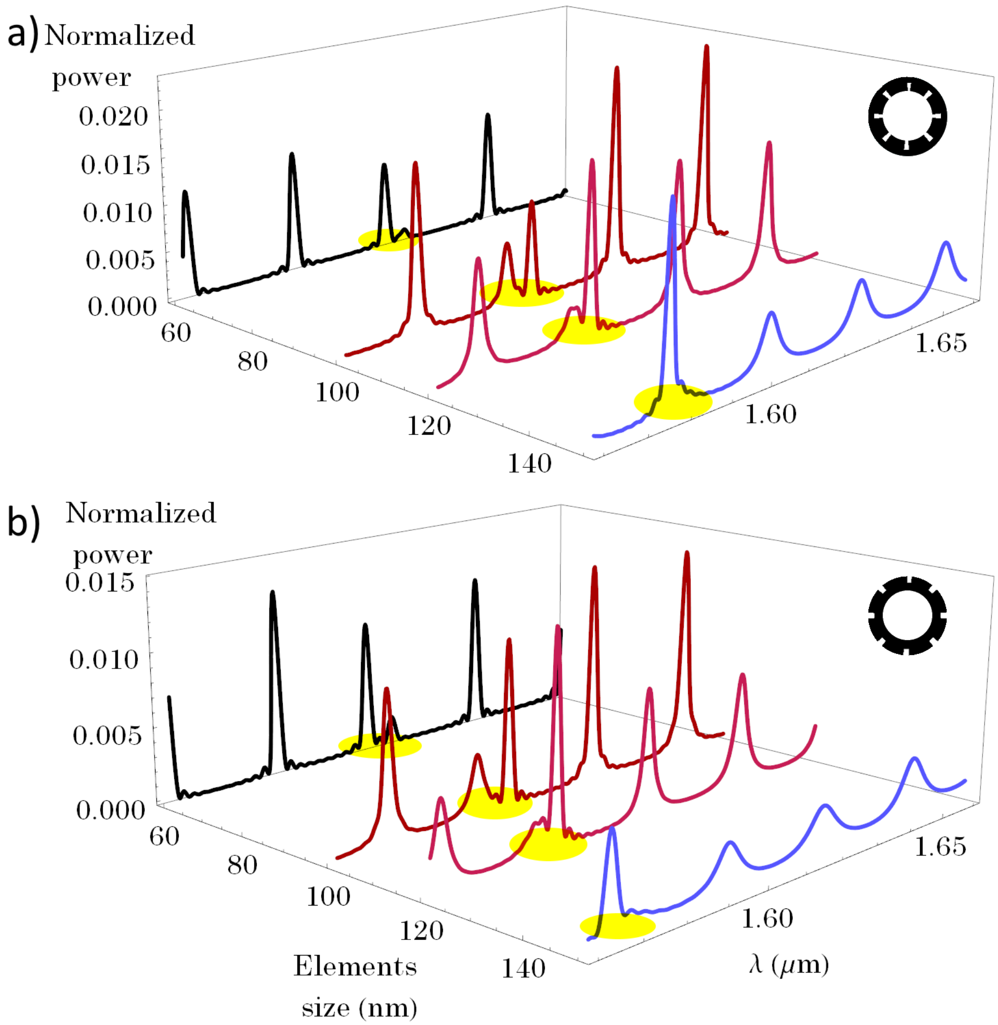

Figure 3.4.: The power spectrum scattered above the angular grating, normalized to integrated power P_o, for angular gratings with dents elements of different sizes (60 nm, 100 nm, 120 nm and 150 nm). There are a) inner wall and b) outer wall gratings. The yellow marks highlight the $l = 0$ resonance peaks. The resonance peaks shift with the elements size as it modifies the effective index. The response is more chaotic than for teeth elements, and the mode splitting is very apparent at the $l = 0$ resonance. These splittings grow with the elements' size. At 150 nm, the elements perturb too much the ring modes and the radiated power is decreased.

3.2. Convergence test

These FDTD simulations were all performed using the automatic non-uniform mesh of Lumerical. The mesh size is controlled by a slider that takes an integer value between 1 and 8: 1 corresponds to the most coarse mesh and fastest simulation, while 8 corresponds to the finest mesh and slowest simulation. Essentially, the number of mesh points per wavelength increases by 4 per slider value, starting at 6 for a slider value of 1. Our simulations were performed at a mesh slider value of 4 to have a good compromise between computation time and data accuracy. To ensure that our results are sufficiently accurate at that mesh size, we must perform a convergence test.

Figure 3.5 shows how the scattered power spectrum above an angular grating change with the slider value. At a slider value of 5, the computation time for this simulation is too high to be included in the convergence test. At slider values of 1 and 2, the spectra are completely different from the slider value 4 spectrum. At a slider value of 3, the spectrum is already very close to the spectrum of the slider value 4. The mean absolute difference between the spectra of slider value 4 and each other slider values are shown in Fig. 3.6. Since the difference between slider value 3 and 4 is so small, we are confident that errors caused by the mesh size must be negligible.

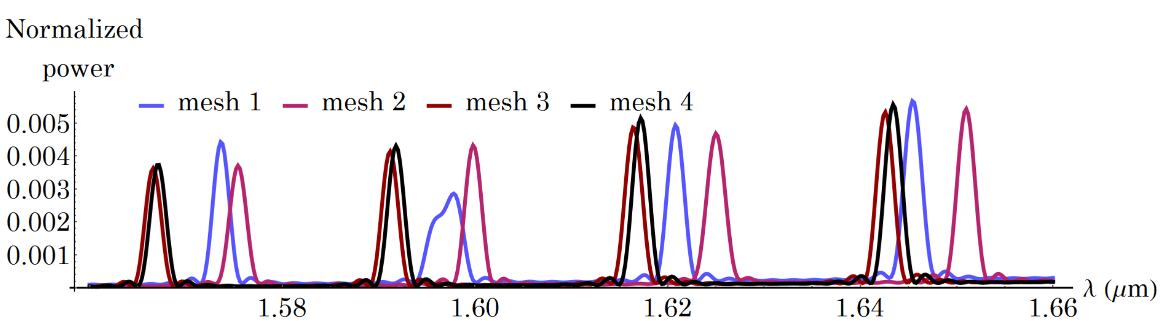

Figure 3.5.: The power spectrum scattered over an angular grating for different FDTD simulation mesh sizes. A higher slider value means a finer mesh. The slider values 1 and 2 are very different, while slider values 3 and 4 converges. The slider value 4 has been used for all the simulations in this thesis.

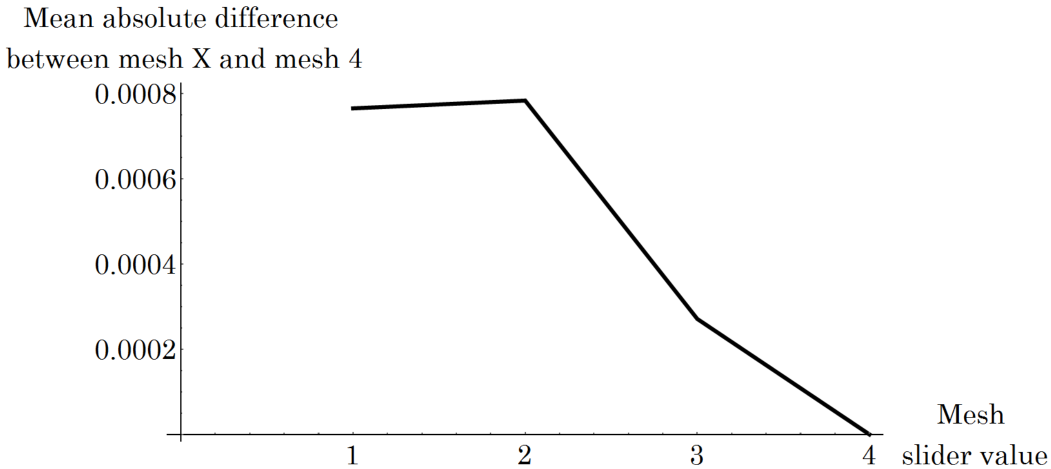

Figure 3.6.: The mean absolute error between the spectra of slider value 4 and all the other slider values seen in Fig. 3.5. Slider values 1 and 2 have large errors while slider value 3 is much closer to 4.

3.3. Single grating

We now proceed to verify Eq. (2.22) from chapter 2, which describes the electrical field scattered from angular gratings, through FDTD simulations. We learned in section 3.1 that "teeth" grating elements are much more efficient than "dents" and will thus only look at the former. We start with the case of the angular grating with a single grating.

The grating is set to 38 square-shaped outer elements of sides of 60 nm, and the gap size between the access waveguide and the ring to 150 nm. We collect the near-field scattering data on a surface large enough to collect all the significant scattering and at a height about 6 μm above the chip to eliminate all evanescent waves. This data is then post-processed to obtain the far-field radiation. This radiation is measured on a hemispherical surface of 1 m radius, which is then projected on a 2D surface for plot visualization.

We compare the far-field intensity and phase from the FDTD simulations and Eq. (2.22) derived from the discrete dipole approximation. First, we look at the total intensity in Fig. 3.7, and then separate the left circular polarization (LCP) and the right circular polarization (RCP) in Fig. 3.8 and Fig. 3.9, respectively, for a clearer understanding of the phase distributions.

As shown in chapter 2, each resonance of the ring scatters a different OAM state, given by

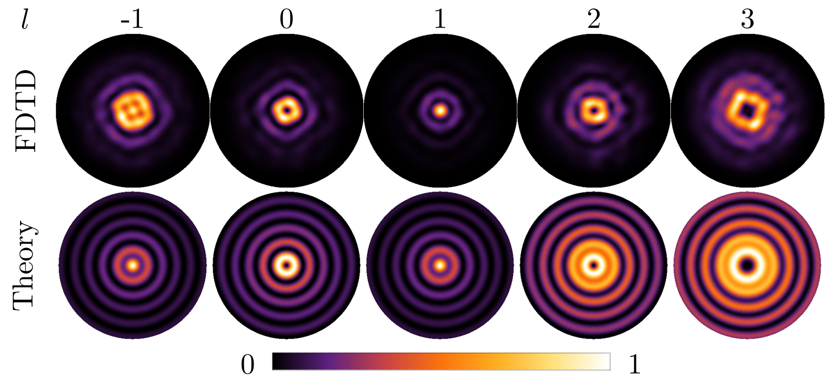

Figure 3.7.: The total far-field radiation intensity for an angular grating with a single grating on the outer wall with $q = 38$, calculated from FDTD and theory (Eq. (2.22)). The $l = 0$ state intensity profiles are doughnut-shaped while the $l = \pm 1$ states intensity is on the propagation axis. This response reveals the vector property of the vortex beams, as uniformly polarized vortex beams have doughnut-shaped intensity profiles for all OAM states except $l = 0$. The difference between the $l = \pm 1$ of the FDTD simulations is due to the scattering powers being different for LCP and RCP.

$l = p - gq$, where p is the ring mode number, g is the diffraction order and q is the number of grating elements. For all of our angular gratings, the parameters are such that $g = 1$. This l state is for the total vector vortex beam, which is in radial and azimuthal polarizations. However, as seen in Eq. (2.22), the l state is different in the circular polarization basis: the OAM states for the LCP and RCP are $l_{\mathrm{L}} = l - 1$ and $l_{\mathrm{R}} = l + 1$, respectively.

The FDTD simulations of Fig. 3.7 to Fig. 3.9 follow well the theory described in section 2.2.3. In Fig. 3.7, we notice that the $l = 0$ state intensity profile is doughnut-shaped while the $l = \pm 1$ states intensities are on the propagation axis, a property that only vector vortex beams can have, as uniformly polarized vortex beams have doughnut-shaped intensity profiles for all OAM states except $l = 0$. The intensity of the $l = 1$ state in LCP in Fig. 3.8 and $l = -1$ state in RCP in Fig. 3.9 (or $l_{\mathrm{L}} = l_{\mathrm{R}} = 0$) are on the propagation axis and correspond to the state without OAM (for the respective polarizations). The other states have doughnut-shaped intensity profiles of increasing radius. The dimmer surrounding rings are due to the Bessel function oscillating over the radius ρ. All the phase profiles in LCP (RCP) go from 0 to 2π l_{L} (l_{R}) times in one revolution of azimuthal angle ϕ and the direction of the rotation switches for negative l_{L} (l_{R}). The theoretical phase also has

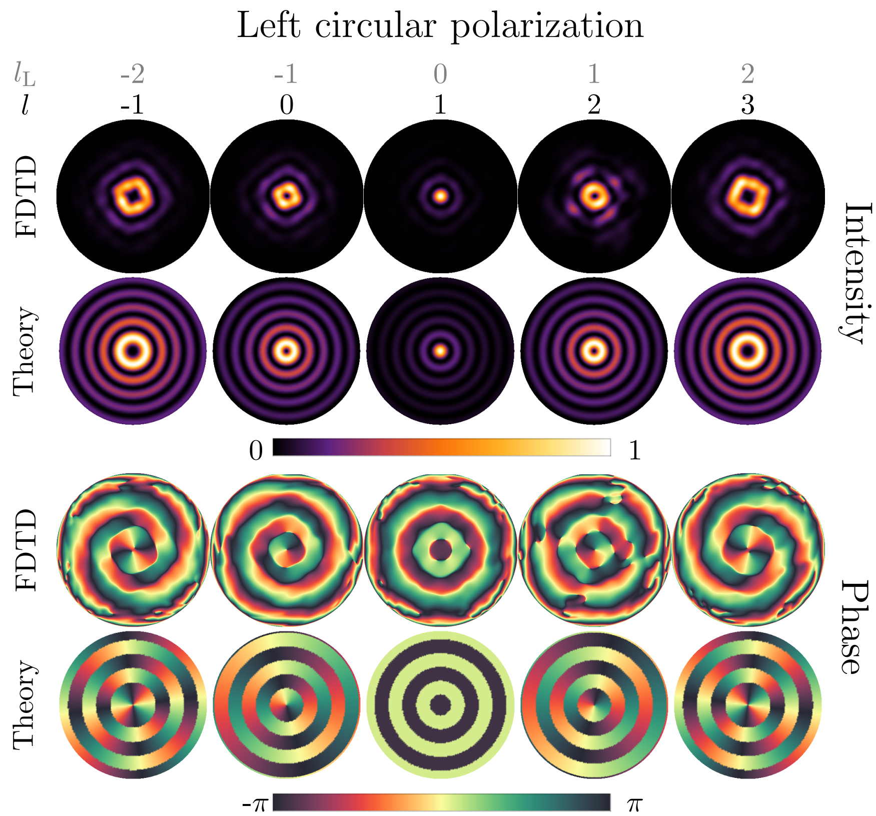

Figure 3.8.: The far-field radiation intensity and phase profiles for the LCP, from FDTD simulations and theory (Eq. (2.22)), for an angular grating with a single grating on the outer wall with $q = 38$. The OAM state for this polarization is $l_{\mathrm{L}} = l - 1$ and so the intensity is non-zero on the propagation axis for $l = 1$ only. The intensity from FDTD follows well the theory, including the surrounding minor rings. The simulated phase shows a different dependence over radius ρ than the theoretical phase. This is likely due to the simulation having an aspherical phase front. The abrupt shifts in the theoretical phase are due to the Bessel function oscillating around 0. In the FDTD simulations, at least the shift closest to the centre is visible. Otherwise, the phase's number of rotations and direction is the same with both method.

abrupt shifts due to the Bessel function oscillating around zero, as a negative amplitude causes a π phase shift. This discontinuity in phase is possible because the intensity is zero at these shift locations. The shifts are also seen in FDTD, notably the one closest to the centre.

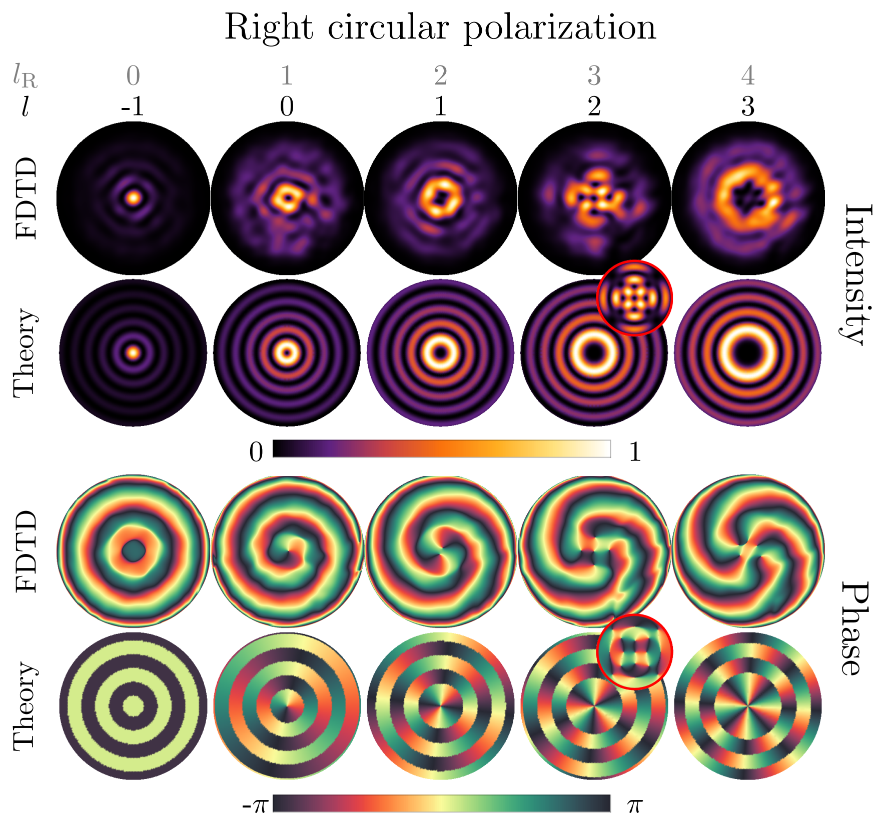

Figure 3.9.: The far-field radiation intensity and phase profiles as in Fig. 3.8 but for the RCP. The OAM state for this polarization is $l_{\mathrm{R}} = l + 1$ as as per Eq. (2.22) and so the intensity is non-zero on the propagation axis for $l = -1$ only. The intensity from FDTD follows well the theory except for $l = 2$, which matches better a superposition of OAM state of $l = \pm 2$, as seen in the insets. The phase from FDTD follows well the theory except for details discussed in the caption of Fig. 3.8.

However, there are a few explainable discrepancies. We notice that the theory lacks some ρ dependent variation (except for the Bessel π jumps) compared to the simulations. For example, for $l = 1$ in LCP in Fig. 3.8 and $l = -1$ for RCP in Fig. 3.9 (or $l_{\mathrm{L}} = l_{\mathrm{R}} = 0$), the FDTD phases have a gradient over ρ while the theoretical phases only switches between two values. While the theoretical phase has a perfect spherical phase front in far-field, the simulation, which takes more information into account such as the material of the ring besides the grating, could have an aspherical phase front. This is reasonable as a difference by a fraction of a wavelength from the spherical shape is enough to create this pattern. Finally, the $l = 2$ state in RCP for FDTD is very different from theory. In fact, the radiation closely matches a superposition state of $l = \pm 2$, as shown in the insets. This can happen if a contra-propagating wave is present in the ring. This effect is not expected and would require further examination to explain. This contrapropagating mode is likely created by a reflection in the grating.

3.4. Double grating

We next add a second grating to the ring resonator in order to generate a superposition of vortex beams, as this superposition is required to use OAM in the quantum key distribution BB84 protocol [2]. We analyze these angular gratings the same way as we did for the single grating in section 3.3. We fix the number of elements of the inner grating at $q_1 = 36$ but vary the outer grating from $q_2 = 36$ to $q_2 = 38$, such that we test the cases $\Delta q = 0$ to $\Delta q = 2$. The superposition states will be expressed as $l = \{l_1, l_2\}$.

Figure 3.12 shows the far-field total intensity of the $\Delta q = 0$ to $\Delta q = 2$ cases, calculated from Eq. (2.22) and FDTD simulations. We will later inspect the LCP and RCP of the $\Delta q = 2$ case in Fig. 3.10 and Fig. 3.11, respectively. We will see in the latter figures that the LCP and RCP patterns from FDTD each differs from theory by opposite rotation shifts. The theoretical patterns of Fig. 3.12 have been corrected for such rotation shifts, and the FDTD simulations follow well the theory in that case. The radiation from the $\Delta q = 0$ angular grating in Fig. 3.12 is similar to the radiation of a single grating, as the second grating simply amplifies the scattering. It is important to specify that the elements of both gratings must perfectly align, otherwise the scattering is weakened by destructive interference, as can be deduced from Eq. (2.27). If such destructive interference were occurring, the scattering would not be completely cancelled as the gratings have different radii. If two gratings of the same radius differs by π/q rotation, the effect is the same as having a single grating of $2q$ elements, thus replacing the generated OAM state $l = p - q$ by $l = p - 2q$. The FDTD simulation of the $l = \{-2, -2\}$ state looks different from theory but it can be described with contra-propagating modes, as it was the case with the single grating RCP with $l = 2$. The $\Delta q = 1$ and $\Delta q = 2$ case show patterns that are not doughnut-shaped since the device is no longer rotationally symmetric.

Figures 3.10 and 3.11 show the far-field intensity and phase profiles of the $\Delta q = 2$ case, for the LCP and RCP, respectively. The FDTD simulations follow well the theory except for a rotation shift of about 45 degrees, counterclockwise for the LCP and clockwise for the RCP. We have $\Delta q = 2$ and so $\Delta l = 2$, meaning that there are two bright spots in one revolution of azimuthal angle. To distinguish and compare the phase profiles, one can use the phase singularities and discontinuities (in other words, undefined phase points and lines) where the intensity is zero. For $l_{\mathrm{L,R}} = \{1, -1\}$, the profile has a central dark line with opposite phase on each side. All profiles of superposition states not carrying $l_{\mathrm{L,R}} = 0$ have a phase singularity on the propagation axis, and so a zero intensity centre. The phase profile of the $l_{\mathrm{L,R}} = \{0, \pm 2\}$ superpositions have a diamond-shaped area on the propagation axis where the phase is nearly constant and each corner is a phase singularity.

We know that the addition of a second grating breaks the rotational symmetry of the structure and thus the exact rotational position of one grating relative to the other is important. Specifically, the rotation of one grating relative to the other rotates the intensity profile as derived in Eq. (2.27). This is demonstrated in Fig. 3.13 where we use the example of the RCP of the $l = \{0, 2\}$ superposition state of the $\Delta q = 1$ angular grating to clearly show the rotation. A rotation by $\phi_{2,o}$ of the outer grating, while keeping the inner grating at a constant $\phi_{1,o} = 0$, rotates the pattern by $\Delta(q_2\phi_{2,o})/\Delta q$.

In summary, the FDTD simulations for double gratings follow well the theoretical radiation patterns, which assume the superposition of single gratings radiation (see Eq. (2.27)). We can thus be confident that a real-life angular grating can generate a superposition of vortex beams.

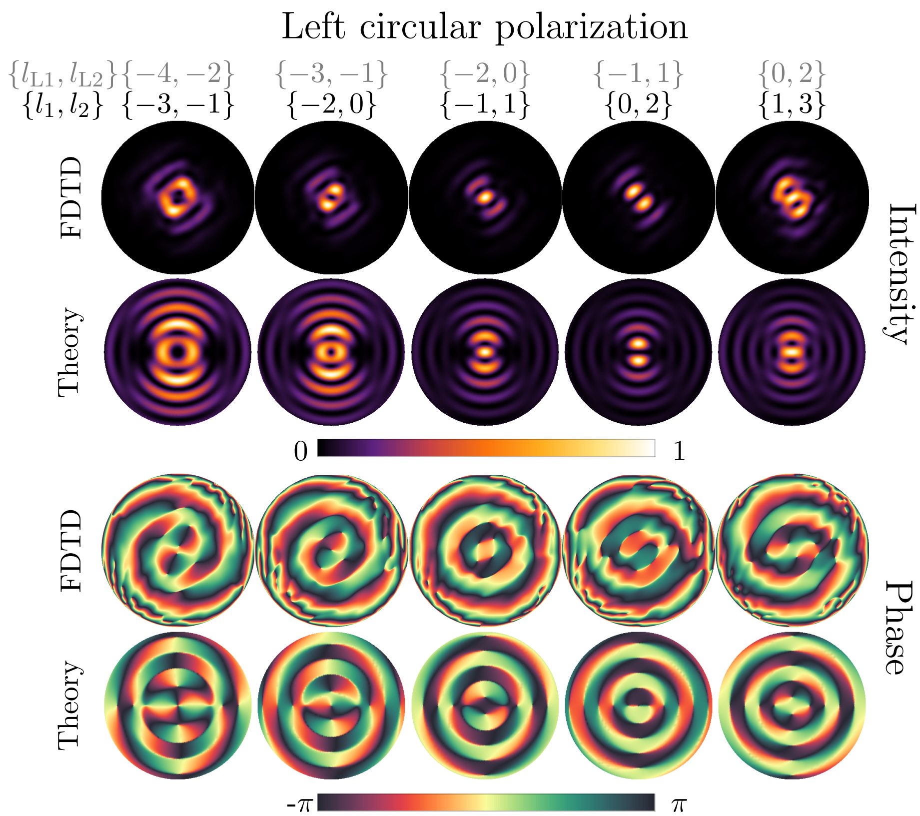

Figure 3.10.: The far-field radiation intensity and phase profiles for the LCP, for FDTD simulations and theory (Eq. (2.22)), with a $\Delta q = 2$ angular grating. The FDTD simulations follow well the theory except for a rotation shift of about 45 degrees counterclockwise.

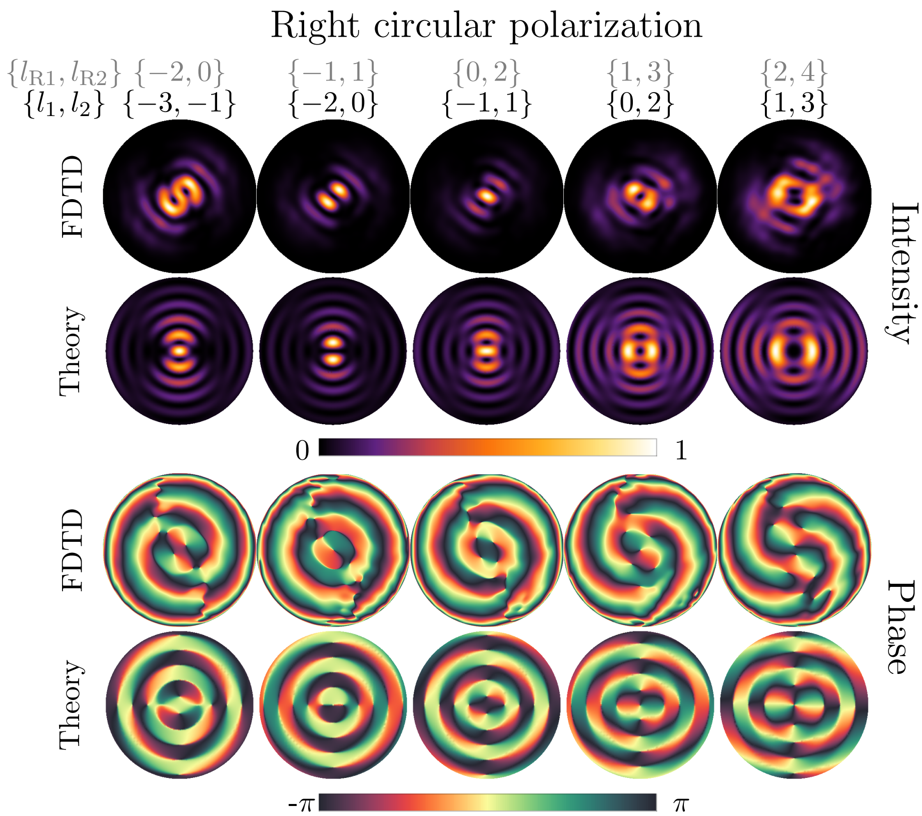

Figure 3.11.: The far-field radiation intensity and phase profiles as in Fig. 3.10 but for the RCP. The FDTD simulations follow well the theory except for a rotation shift of about 45 degrees clockwise.

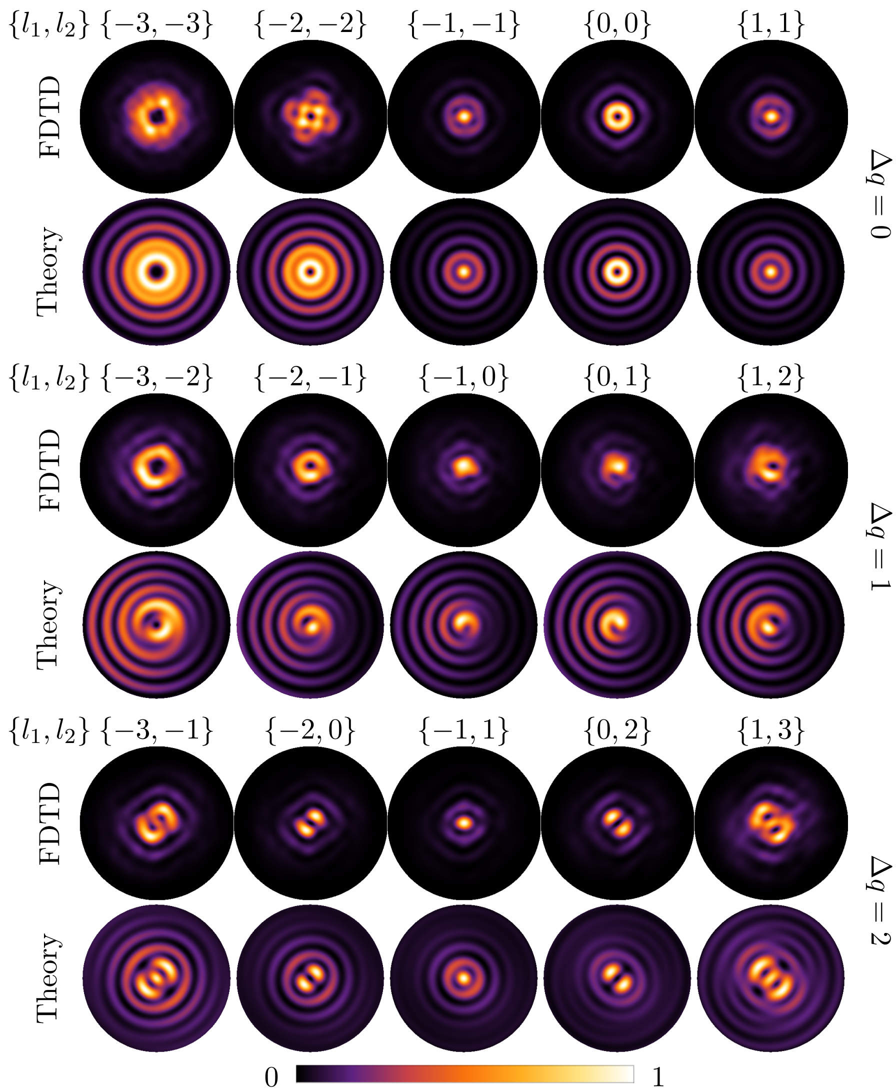

Figure 3.12.: The far-field total intensity for angular gratings with $\Delta q = 0$ to $\Delta q = 2$. The rotation of the theoretical patterns has been corrected for each circular polarization, as the differences can be seen in Fig. 3.10 and Fig. 3.11. The FDTD simulations follow well the theory.

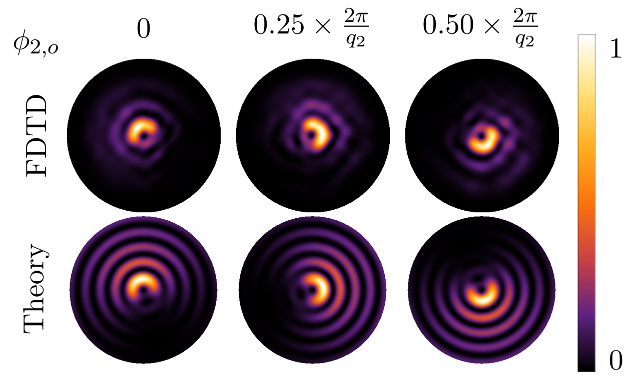

Figure 3.13.: The far-field intensity profile pattern rotation, as the outer grating rotates by $\phi_{2,o}$ and the inner grating is fixed at $\phi_{1,o} = 0$, using for this example the superposition state $l = \{0, 2\}$ in RCP of a $\Delta q = 1$ angular grating. After a rotation of $2\pi/q_2$ radians, the grating returns to its initial position. The rotation of the first theoretical profile ($\phi_{2,o} = 0$) is corrected to match the FDTD for clarity. We see that each subsequent grating rotation of $0.25 \times 2\pi/q_2$ gives a pattern rotation of $\pi/2$.

3.5. Conclusion

We have confirmed that the electric field equation for the scattering of angular gratings found in chapter 2 describes well reality with FDTD simulations, even though the theory has a few approximations. We also found optimal parameters for our angular gratings to maximize the vortex beams power, in particular the gap size between the ring and access waveguide and the grating elements size. This information will be useful for the next chapter where we fabricate and characterize angular gratings.

4. Experiment

Now that we presented the analytical model of the angular grating scattering and confirmed it with simulations, the last step is to fabricate and characterize the actual device. While we did not fully characterize the device due to technical limitations, the data collected provides us valuable information and lessons for a continuation of this work.

4.1. Fabrication

Our complete nanostructure is composed of an angular grating with an access waveguide between two grating couplers to get light in and out of the chip, as seen in Fig. 4.1. Its fabrication is based on the planar process, developed in 1959 by Fairchild Semiconductor. We start off with a wafer of silicon on silica (SiO_2) substrate. A layer of electron sensitive resist (ZEP 520a) is then added on top through a spin-coating process. This resist is patterned by electron beam (e-beam) lithography. The chip is subsequently plasma etched using a reactive ion etcher, which carves through the area of silicon unprotected by the resist. Finally, the remaining resist is stripped off with acidic solutions. We fabricated the devices according to the design parameters established in chapter 3. The fabrication was performed at the University of Ottawa by members of our group, Dr. Sebastian Schulz and Dr. Jeremy Upham, except for the etching part which was done by Dr. Liam O'Faolain at the University of St Andrews. Figure 4.2 shows the finished product: a 1.5 cm x 1.5 cm chip containing 60 different structures.

The final dimensions of the fabricated angular gratings are different from the ones of the simulated angular gratings. In the simulations, the ring was made as small as possible to decrease the computation time. However, a bigger radius increases the coupling between the ring and access waveguide, as a bigger portion of the ring is close to the waveguide. It also decreases the bending loss as it relaxes the curvature. The radius is thus set to 7.8 μm. Cursory simulations showed that this change in ring radius would not change

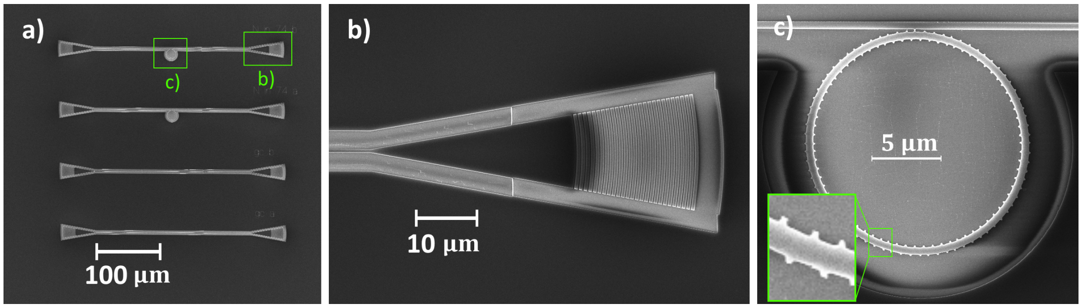

Figure 4.1.: A scanning electron microscope (SEM) view of the fabricated a) reference waveguides and structures composed of b) gratings couplers and c) an angular grating.

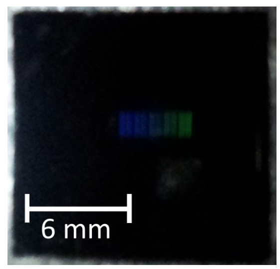

Figure 4.2.: A 1.5 cm x 1.5 cm chip containing 60 different structures, under a white light.

the desired behaviour, but only improves the performance of an actual device. The gap between the ring resonator and the access waveguide is set to around 200 nm, as small as possible without merging with the outer elements of the angular grating (see Fig. 3.1 in section 3.1). To keep the $l = 0$ state around $\lambda = 1550$ nm, the different angular gratings have between 74 and 76 grating elements. The side length of the elements is about 140 nm since, as seen in section 3.1, it is the optimal dimension for maximal scattering without too much mode splitting.

4.1.1. What can go wrong

Since the scale of these structures is extremely small, special care must be given to obtain good quality feature sizes, and thus performance consistent with the design. However, even with the best diligence, there will always be defects in the final product which leads to losses in transmission. This is why a single structure is iterated multiple times to raise the probability of getting a working device.

First, the waveguide dimensions dictate which wavelengths are in a single spatial mode. Having a single mode is important to have the correct mode with optimal coupling between the integrated components. Getting those dimensions wrong could thus easily change the supported wavelength to beyond what we can optically characterize. Secondly, the quality of the plasma etch will determine how smooth and vertical the side walls of the structure become. Poor verticality will affect the modes carried by the device and how they behave, while the roughness of the side walls will lead to scattering and thus a more lossy device [57]. During the etching process, one thus aims for smooth walls. Thirdly, the dimensions of the grating couplers, such as its periodicity and grating depth, vary its effective refractive index and thus its centre of coupling bandwidth (see section 2.1). Fourthly, the gap between the ring and the waveguide dictates how well the light couples (see Fig. 3.1 in section 3.1). Because this gap is a narrow feature, it is highly sensitive to error or variations during the lithography and etching steps. For the angular grating, the size of the grating elements affects their scattering strength (see section 2.2.3).

Finally, the e-beam writing field is about 100 μm x 100 μm large. For bigger structures, the stage needs to move. If not done accurately, the patterns before and after the move ends up misaligned. This process of aligning the stage movements is called write-field alignment and errors caused by misalignment between write-fields are called stitching errors. The waveguide of our structure is over 200 μm long and so the different regions need to be stitched together. When the waveguide end up misaligned, this abrupt change causes reflection in the waveguide, leading to Fabry-Perot oscillations in the transmitted spectrum, or in the worst cases, no transmission at all. We want to minimize the Fabry-Perot oscillations as too much can hide the signal for which we are looking.

4.2. Characterization

As the structure is a few microns wide, we need a microscope to image it and align fibre ends on the grating couplers. While commercial microscopes are widely available, those are usually enclosed and fixed in a vertical direction. However, we want to eventually be able to perform operations on the light emitted out of the rings, for example to do interferometry to measure the phase front. Therefore, we built a set-up with the sample mounted on it's

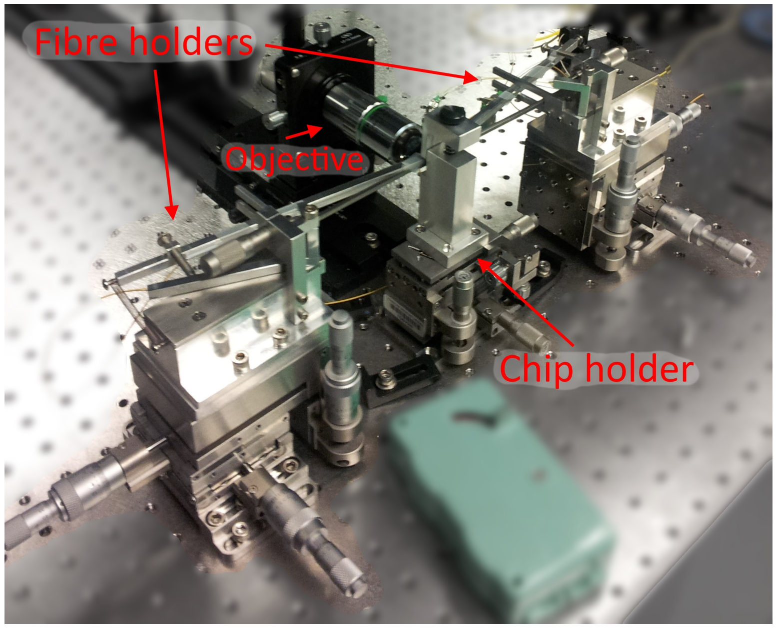

Figure 4.3.: The custom-made holders for the chip and fibres, placed over 5-axes and 3-axes stages, respectively.

side, so that its emission is level with the optical table surface.

I designed custom-made holders for the chip and the fibres, as seen in Fig. 4.3, inspired from a design of Bruck *et al.* [58]. The chip is held in place on its side with a light pressure of a screw. The fibre holders have a movable arm that allows us to precisely set the angle of the fibre end over the chip, as this angle changes the centre bandwidth of the grating couplers (section 2.1). We set the fibres (input and output) at about 10 degrees off the normal of the chip to avoid second-order reflection in the grating. The angle of the arm is set with a micrometer, and the fibre holder converts the linear motion of the micrometer to a rotational motion of the arm. Furthermore, the pivot point of the arm must be placed as close as possible to the fibre end, in order to mitigate how the fibre end moves closer to or away from the chip as its angle is changed. The arms must also be sufficiently narrow to fit with a fibre in the 1.2 cm between the chip and our 100x magnification objective, but also sufficiently thick to be stable within a micron to vibrations. The fibre holders are placed on 3-axes translation stages, while the chip holder is placed on a 5-axes stage to control in addition its pitch and roll.

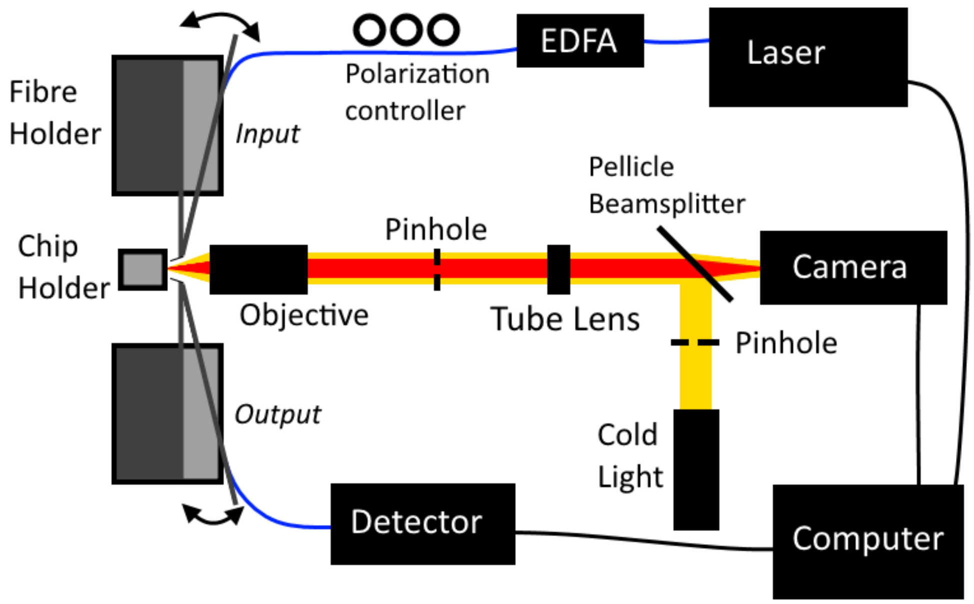

Figure 4.4.: The set up of the experiment is mostly a horizontal microscope. The red light is the laser infrared light radiated by the nanostructure while the yellow light is the cold (visible) light used to image the nanostructure. The blue lines are optical fibres while the black lines are cables linking the instruments to the computer.

Figure 4.4 shows the set up for characterizing the angular gratings. The infrared light source is a Koshin laser with a narrow bandwidth (100 kHz) which can sweep from a wavelength of 1525 nm to 1630 nm. However, its maximum output power of 1 mW is too weak to be detected after the losses through the nanostructures. We amplify the laser source with an erbium-doped fibre amplifier (EDFA) to bring the power to around 10 mW. The orientation of the linear polarization of the laser is optimized with a polarizer in order to get a TE mode in the integrated waveguide (section 2.2.3). This light is passed to one of the fibre holders where the bare end of the fibre is aligned over a grating coupler.

A second fibre captures the light out of the output grating coupler. This measures the transmission through the waveguide, as seen in Fig. 4.5. While we ultimately want to image the radiation from the angular gratings, the transmission measurement is required to align the fibres over the grating couplers and find the location of the ring resonances in the spectrum. Of all the structures on the chip, we focus on two that seem to work well: an

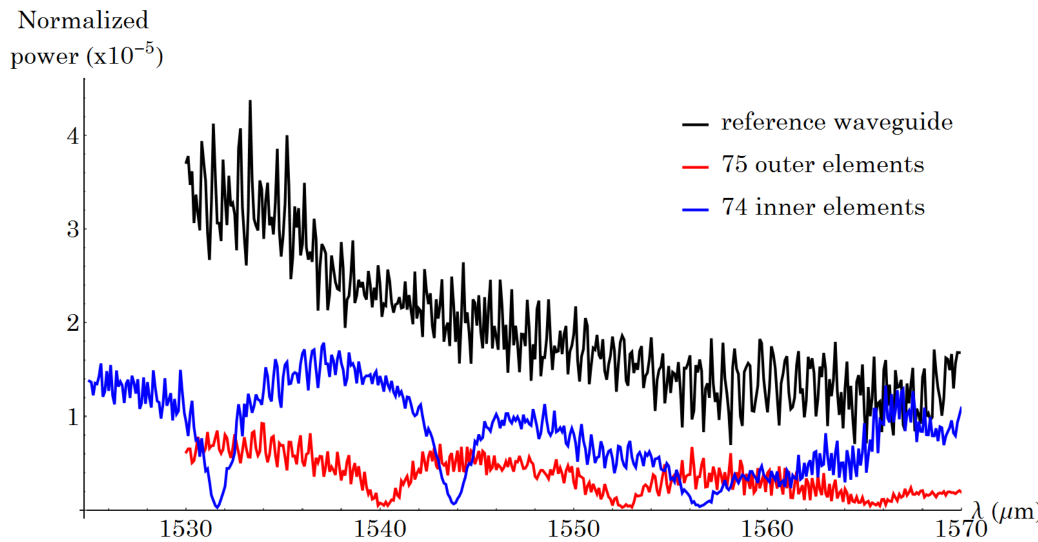

Figure 4.5.: Three transmission spectra of different structures. The black curve is a reference waveguide without angular grating to gauge the coupling bandwidth of the grating couplers. The oscillations are due to Fabry-Perot resonances between the two grating couplers. The blue and red curves are from angular gratings with 75 outer and 74 inner elements, respectively. The sudden dips in transmission occur at the resonance wavelengths of the ring resonator and so where possible vortex beams are generated.

angular grating with 74 inner elements and the other one with 75 outer elements. Figure 4.5 shows the transmission of these two structures and a reference waveguide, without a ring resonator (black curve). We see from the reference waveguide that we are on the red side of the grating couplers bandwidth, which can explain the overall low transmission (10^{-5}). The sudden dips in the other transmission curves reveal the resonance wavelengths of the ring resonators. For the 74 inner elements grating (blue curve), the dips are around 1532, 1544 and 1556 nm, and for the 75 outer elements (red curve), around 1540, 1552 and 1566 nm. Those dips can shift slightly with time as the chip oxidizes or absorbs humidity, which changes its effective index.

Once the light is coupled to the integrated structure, the radiation from the angular grating is captured by an objective and a tube lens focuses the light into an infrared camera. The imaging of the structures themselves, as seen in Fig. 4.6, is done with the same set up except that a cold light is inserted in the beam path with a pellicle beamsplitter.

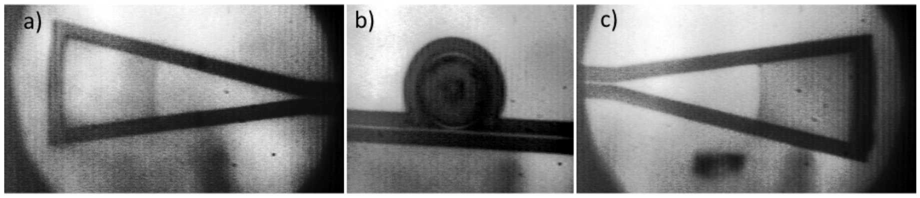

Figure 4.6.: The a), c) gratings couplers and the b) angular grating, as seen through a 100x objective. The faint vertical lines are artifacts of the camera.

An objective of magnification of 20x (0.42 NA) is sufficient for the alignment process but a magnification of 100x (0.50 NA) is better for the radiation imaging as it removes the surrounding noise. The 100x objectives usually have a working distance of 1 or 2 mm, which is the required distance between the front of the objective and the chip to get a focused image. In our case, we used a 100x objective with a long working distance of 12.0 mm in order to fit the fibre holders arms between the objective and the chip.

While we detect resonance dips in transmission, we cannot confirm the presence of vortex beams by imaging the angular grating radiation, as seen in Fig. 4.7 for the $\lambda = 1540.0$ nm resonance of the 75 outer elements grating and the $\lambda = 1531.2$ nm resonance of the 74 inner elements grating. We can discern a ring pattern but there is a lot of background noise. One reason is that there is a lot of light from the input fibre reflecting on the left side of the structure. Using a 100x objective helps cleaning this noise but it is not enough. To conclusively observe vortex beams, we will need to improve the signal to noise ratio of the scattered light to finally measure its phase front through interferometry.

The laser, detector and camera are all connected to a computer for data acquisition and automation. We use LabVIEW [59] to automate the laser spectrum sweeping and detector data saving.

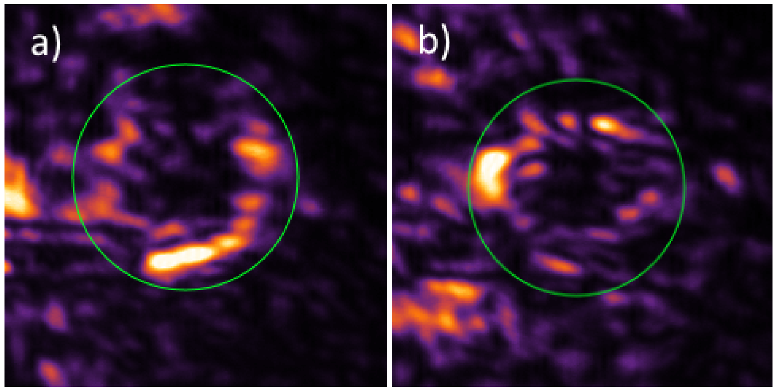

Figure 4.7.: The radiation at resonance from angular gratings with a) 75 outer elements (λ = 1540.0 nm) and b) 74 inner elements (λ = 1531.2 nm). While we can discern a ring pattern in the areas contained by the green circles, there is a lot of background noise, especially at the left from the input fibre. The bright spot just under the ring comes from the gap between the angular grating and the waveguide where light couples.

4.3. How to improve the experiment

While we could not image the vortex beam from our angular gratings, some modifications to the structures would ease the task. First, we could extend the waveguide length to reduce the noise from the input fibre reflected light. The current waveguide length on each side of the ring resonator is about 120 µm. Doubling this length should be sufficient to neglect the reflected light background noise. We could also add a ring resonator without gratings to the chip in order to compare the width of the dips (or the Q factor) so we could tell whether the gratings are scattering well (section 2.2.1). We also learned afterwards that the silicon layer thickness is about 20 nm shorter than we thought. This does not change the workings of the angular gratings, but it shifts the operating bandwidth of the grating couplers. Therefore, we could either choose another wafer with the desired thickness or change the design of the grating couplers to be optimized for the actual silicon layer thickness.

We could also try different approaches. We could optimize the angle of the fibres over the grating couplers. Since bringing a fibre angle closer to the normal of the chip red-shifts the coupling bandwidth, this could increase the overall transmission of the structure. Finally, we could perform the reverse process: generate a vortex beam by other means and try to couple it to an angular grating. Since angular gratings can act as sorters of OAM, a vortex beam with the right l state at the right wavelength will couple all the way through the waveguide where we can detect it.

4.4. Conclusion

We fabricated angular gratings according to our designs and built a set up to measure their transmission spectra. We saw dips in the spectra that reveal the resonance wavelengths of the rings, which are also the wavelengths where vortex beams can be generated. Unfortunately, the imaging of the vortex beams proved to be difficult due to a noisy background. The next steps are to fabricate improved version of our structures, such as lengthening the waveguides to reduce the scattered light from the input fibre, and try different techniques such as sorting a vortex beam instead of imaging the generation of one.

A. Appendix

This appendix provides more details on our custom-made fibre holders that were used for the experiment. These fibre holders let one precisely set the angle at which a fibre end points, which is very important to couple optimally with grating couplers.

Figure A.1 shows how the fibre holder moves. The device can be divided into three parts: a micrometer holder, a lever and an arm. The fibre is glued on the arm, and a spring keeps that arm closed. To open it, the micrometer pushes on the lever which in turn pushes on the arm. This lever is important as it increases the arm angle range for the same micrometer travel range. Using a micrometer directly on the arm would require a very long arm, which would make the arm prone to vibration. The relation between the micrometer travel distance and the fibre angle is nonlinear but it can be calibrated. For example, one can use visible light in the fibre and measure, on a surface at some distance, the deviation of the spot from the centre line for different micrometer travel distances.

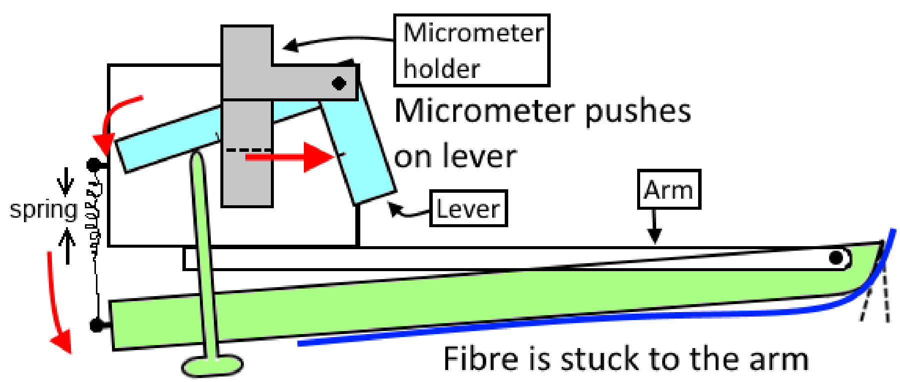

Figure A.1.: A top view of the fibre holder when open. The angle of the fibre can be precisely set with a micrometer. A spring holds the arm closed. To open the arm, the micrometer pushes on a lever which in turn pushes on the arm.

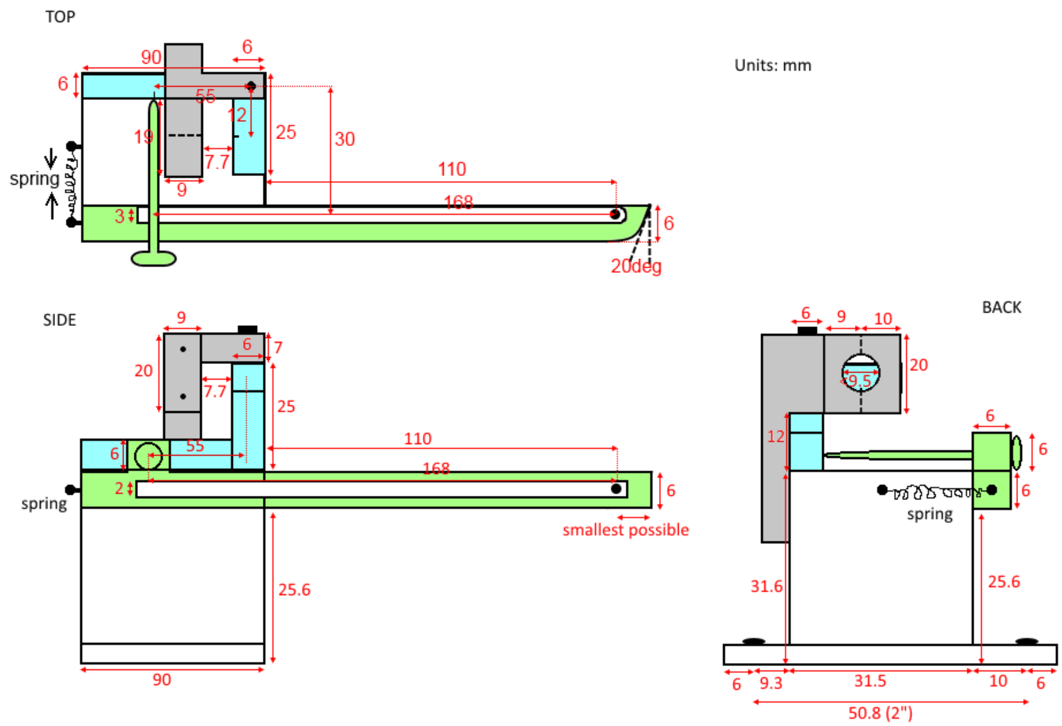

Figure A.2.: The fibre holders with dimension, as seen from the top, side and back.

On Fig. A.2 are the sketches of the fibre holder with its dimensions. The arm is fairly long as we needed space between the fibre holder and the sample for other optical components. Shorter arms would improve the stability of the fibre end position. Moreover, the pivot point on the arm must be placed as close to end as possible to reduce the arm rotation effect on the fibre end position.

Bibliography

[1] N. R. Heckenberg, R. McDuff, C. P. Smith, and A. G. White, "Generation of optical phase singularities by computer-generated holograms," *Optics Letters*, vol. 17, pp. 221–223, 1992.

[2] R. W. Boyd, A. Jha, M. Malik, C. O'Sullivan, B. Rodenburg, and D. J. Gauthier, "Quantum key distribution in a high-dimensional state space: exploiting the transverse degree of freedom of the photon," vol. 7948, p. 79480L, Proceedings of SPIE, 2011.

[3] X. Cai, J. Wang, M. J. Strain, B. Johnson-Morris, J. Zhu, M. Sorel, J. L. O'Brien, M. G. Thompson, and S. Yu, "Integrated Compact Optical Vortex Beam Emitters," *Science*, vol. 338, pp. 363–366, Oct. 2012.

[4] J. Kepler, *De cometis libelli tres*. 1619.

[5] M. Padgett and R. Bowman, "Tweezers with a twist," *Nature Photonics*, vol. 5, pp. 343–348, June 2011.

[6] L. Allen, M. W. Beijersbergen, R. J. C. Spreeuw, and J. P. Woerdman, "Orbital angular momentum of light and the transformation of Laguerre-Gaussian laser modes," *Physical Review A*, vol. 45, pp. 8185–8189, 1992.

[7] H. He, M. Friese, N. Heckenberg, and H. Rubinsztein-Dunlop, "Direct Observation of Transfer of Angular Momentum to Absorptive Particles from a Laser Beam with a Phase Singularity," *Physical Review Letters*, vol. 75, pp. 826–829, July 1995.

[8] N. Simpson, K. Dholakia, L. Allen, and M. J. Padgett, "Mechanical equivalence of spin and orbital angular momentum of light: an optical spanner," *Optics Letters*, vol. 22, pp. 52–54, Jan. 1997.

[9] A. T. O'Neil, I. MacVicar, L. Allen, and M. J. Padgett, "Intrinsic and Extrinsic Nature of the Orbital Angular Momentum of a Light Beam," *Physical Review Letters*, vol. 88, no. 053601, 2002.

[10] J. Leach, H. Mushfique, R. di Leonardo, M. Padgett, and J. Cooper, "An optically driven pump for microfluidics," *Lab on a Chip*, vol. 6, pp. 735–739, 2006.

[11] J. Courtial, K. Dholakia, D. A. Robertson, L. Allen, and M. J. Padgett, "Measurement of the rotational frequency shift imparted to a rotating light beam possessing orbital angular momentum," *Physical Review Letters*, vol. 80, pp. 3217–3219, 1998.

[12] M. P. J. Lavery, F. C. Speirits, S. M. Barnett, and M. J. Padgett, "Detection of a Spinning Object Using Light's Orbital Angular Momentum," *Science*, vol. 341, pp. 537–540, 2013.

[13] L. Marrucci, "Spinning the Doppler Effect," *Science*, vol. 341, pp. 464–465, 2013.

[14] D. B. Phillips, M. P. Lee, F. C. Speirits, S. M. Barnett, S. H. Simpson, M. P. J. Lavery, M. J. Padgett, and G. Gibson, "Rotational Doppler velocimetry to probe the angular velocity of spinning microparticles," *Physical Review A*, vol. 90, no. 011801R, 2014.

[15] H. He, N. Heckenberg, and H. Rubinsztein-Dunlop, "Optical Particle Trapping with Higher-order Doughnut Beams Produced Using High Efficiency Computer Generated Holograms," *Journal of Modern Optics*, vol. 42, pp. 217–223, Jan. 1995.

[16] K. T. Gahagan and G. A. Swartzlander, "Optical vortex trapping of particles," *Optics Letters*, vol. 21, pp. 827–829, 1996.

[17] V. Shvedov, A. R. Davoyan, C. Hnatovsky, N. Engheta, and W. Krolikowski, "A long-range polarization-controlled optical tractor beam," *Nature Photonics*, vol. 8, pp. 846–850, Nov. 2014.

[18] S. W. Hell and W. Jan, "Breaking the diffraction resolution limit by stimulated emission: stimulated-emission-depletion fluorescence microscopy," *Optics Letters*, vol. 19, pp. 780–782, 1994.

[19] T. A. Klar, E. Engel, and S. W. Hell, "Breaking Abbe's diffraction resolution limit in fluorescence microscopy with stimulated emission depletion beams of various shapes," *Physical Review E*, vol. 64, no. 066613, 2001.

[20] K. I. Willig, S. O. Rizzoli, V. Westphal, R. Jahn, and S. W. Hell, "STED microscopy reveals that synaptotagmin remains clustered after synaptic vesicle exocytosis," *Nature*, vol. 440, pp. 935–939, Apr. 2006.

[21] S. Quabis, R. Dorn, M. Eberler, O. Glöckl, and G. Leuchs, "Focusing light to a tighter spot," *Optics Communications*, vol. 179, pp. 1–7, May 2000.

[22] R. Dorn, S. Quabis, and G. Leuchs, "Sharper Focus for a Radially Polarized Light Beam," *Physical Review Letters*, vol. 91, no. 233901, 2003.

[23] H. Dehez, M. Piché, and Y. De Koninck, "Resolution and contrast enhancement in laser scanning microscopy using dark beam imaging," *Optics Express*, vol. 21, pp. 15912–15925, July 2013.

[24] S. Fürhapter, A. Jesacher, S. Bernet, and M. Ritsch-Marte, "Spiral interferometry," *Optics Letters*, vol. 30, pp. 1953–1955, 2005.

[25] G. A. Swartzlander, "Peering into darkness with a vortex spatial filter," *Optics Letters*, vol. 26, pp. 497–499, 2001.

[26] G. Foo, D. M. Palacios, G. A. Swartzlander Jr, and others, "Optical vortex coronagraph," *Optics Letters*, vol. 30, pp. 3308–3310, 2005.

[27] A. E. Willner, H. Huang, Y. Yan, Y. Ren, N. Ahmed, G. Xie, C. Bao, L. Li, Y. Cao, Z. Zhao, and others, "Optical communications using orbital angular momentum beams," *Advances in Optics and Photonics*, vol. 7, pp. 66–106, 2015.

[28] S. Ramachandran, P. Kristensen, and M. F. Yan, "Generation and propagation of radially polarized beams in optical fibers," *Optics letters*, vol. 34, pp. 2525–2527, 2009.

[29] C. H. Bennett and G. Brassard, "Quantum cryptography: public key distribution and coin tossing," in *International Conference on Computers, Systems and Signal Processing*, (Bangalore, India), pp. 175–179, Dec. 1984.

[30] N. J. Cerf, M. Bourennane, A. Karlsson, and N. Gisin, "Security of Quantum Key Distribution Using d -Level Systems," *Physical Review Letters*, vol. 88, Mar. 2002.

[31] M. W. Beijersbergen, R. P. C. Coerwinkel, M. Kristensen, and J. P. Woerdman, "Helical-wavefront laser beams produced with a spiral phaseplate," *Optics Communications*, vol. 112, pp. 321–327, 1994.

[32] G. A. Turnbull, D. A. Robertson, G. M. Smith, L. Allen, and M. J. Padgett, "The generation of free-space Laguerre-Gaussian modes at millimetre-wave frequencies by use of spiral phaseplate," *Optics Communications*, vol. 127, pp. 183–188, June 1996.

[33] H. Li, D. B. Phillips, X. Wang, Y.-L. D. Ho, L. Chen, X. Zhou, J. Zhu, S. Yu, and X. Cai, "Orbital angular momentum vertical-cavity surface-emitting lasers," *Optica*, vol. 2, pp. 547–552, June 2015.

[34] L. Marrucci, C. Manzo, and D. Paparo, "Optical Spin-to-Orbital Angular Momentum Conversion in Inhomogeneous Anisotropic Media," *Physical Review Letters*, vol. 96, no. 163905, 2006.

[35] E. Karimi, S. A. Schulz, I. De Leon, H. Qassim, J. Upham, and R. W. Boyd, "Generating optical orbital angular momentum at visible wavelengths using a plasmonic metasurface," *Light: Science & Applications*, vol. 3, pp. 1–4, May 2014.

[36] S. A. Schulz, T. Machula, E. Karimi, and R. W. Boyd, "Integrated multi vector vortex beam generator," *Optics Express*, vol. 21, pp. 16130–16141, July 2013.

[37] Y. Wang, X. Feng, D. Zhang, P. Zhao, X. Li, K. Cui, F. Liu, and Y. Huang, "Generating optical superimposed vortex beam with tunable orbital angular momentum using integrated devices," *Scientific Reports*, vol. 5, pp. 1–10, July 2015.

[38] H. Li, M. J. Strain, L. Meriggi, L. Chen, J. Zhu, K. Cicek, J. Wang, X. Cai, M. Sorel, M. G. Thompson, and S. Yu, "Pattern manipulation via on-chip phase modulation between orbital angular momentum beams," *Applied Physics Letters*, vol. 107, no. 051102, 2015.

[39] Q. Xiao, C. Klitis, S. Li, Y. Chen, X. Cai, M. Sorel, and S. Yu, "Generation of

photonic orbital angular momentum superposition states using vortex beam emitters with superimposed gratings," *Optics Express*, vol. 24, pp. 3168–3176, Feb. 2016.

[40] C. Brunet, P. Vaity, Y. Messaddeq, S. LaRochelle, and L. A. Rusch, "Design, fabrication and validation of an OAM fiber supporting 36 states," *Optics Express*, vol. 22, pp. 26117–26127, Oct. 2014.

[41] D. Taillaert, W. Bogaerts, P. Bienstman, T. F. Krauss, P. Van Daele, I. Moerman, S. Verstuyft, K. De Mesel, and R. Baets, "An out-of-plane grating coupler for efficient butt-coupling between compact planar waveguides and single-mode fibers," *IEEE Journal of Quantum Electronics*, vol. 38, pp. 949–955, 2002.

[42] D. Rosenblatt, A. Sharon, and A. Friesem, "Resonant grating waveguide structures," *IEEE Journal of Quantum Electronics*, vol. 33, pp. 2038–2059, Nov. 1997.

[43] D. Taillaert, F. Van Laere, M. Ayre, W. Bogaerts, D. Van Thourhout, P. Bienstman, and R. Baets, "Grating couplers for coupling between optical fibers and nanophotonic waveguides," *Japanese Journal of Applied Physics*, vol. 45, pp. 6071–6077, 2006.

[44] A. Yariv, "Universal relations for coupling of optical power between microresonators and dielectric waveguides," *Electronics Letters*, vol. 36, pp. 321–322, 2000.

[45] J. Zhu, X. Cai, Y. Chen, and S. Yu, "Theoretical model for angular grating-based integrated optical vortex beam emitters," *Optics Letters*, vol. 38, pp. 1343–1345, Apr. 2013.

[46] D. J. Griffiths, *Introduction to Electrodynamics*. Prentice Hall, 3rd ed., 1999. pp. 454-457.

[47] W. J. M. Kort-Kamp and C. Farina, "On the exact electric and magnetic fields of an electric dipole," *American Journal of Physics*, vol. 79, pp. 111–114, 2011.

[48] R. Li, X. Feng, D. Zhang, K. Cui, F. Liu, and Y. Huang, "Radially Polarized Orbital Angular Momentum Beam Emitter Based on Shallow-Ridge Silicon Microring Cavity," *IEEE Photonics Journal*, vol. 6, pp. 1–10, June 2014.

[49] T. J. Kippenberg, "Microresonators: particle sizing by mode splitting," *Nature Photonics*, vol. 4, pp. 9–10, 2010.

[50] Q. Huang, K. Ma, and S. He, "Experimental Demonstration of Single Mode-Splitting in Microring With Bragg Gratings," *IEEE Photonics Technology Letters*, vol. 27, pp. 1402–1405, July 2015.

[51] C. E. Campanella, A. Giorgini, S. Avino, P. Malara, R. Zullo, G. Gagliardi, and P. De Natale, "Localized strain sensing with fiber Bragg-grating ring cavities," *Optics Express*, vol. 21, pp. 29435–29441, Dec. 2013.

[52] J. Čtyroký, I. Richter, and M. Šiňor, "Dual resonance in a waveguide-coupled ring microresonator," *Optical and Quantum Electronics*, vol. 38, pp. 781–797, 2006.

[53] M. W. Puckett, F. Vallini, A. Grieco, and Y. Fainman, "Multichannel Bragg gratings in silicon waveguides with asymmetric sidewall modulation," *Optics Letters*, vol. 40, pp. 379–382, Feb. 2015.

[54] "Lumerical Solutions, Inc." http://www.lumerical.com/tcad-products/fdtd/.

[55] J. B. Schneider, "Understanding the Finite-Difference Time-Domain Method." http://www.eecs.wsu.edu/ schneidj/ufdtd, 2010.

[56] C.-S. Ma, X. Yan, Y.-Z. Xu, Z.-K. Qin, and X.-Y. Wang, "Characteristic Analysis of Bending Coupling Between Two Optical Waveguides," *Optical and Quantum Electronics*, vol. 37, pp. 1055–1067, Sept. 2005.

[57] K. Solehmainen, T. Aalto, J. Dekker, M. Kapulainen, M. Harjanne, K. Kukli, P. Heimala, K. Kolari, and M. Leskelä, "Dry-etched silicon-on-insulator waveguides with low propagation and fiber-coupling losses," *Journal of lightwave technology*, vol. 23, pp. 3875–3880, 2005.

[58] R. Bruck, B. Mills, B. Troia, D. J. Thomson, F. Y. Gardes, Y. Hu, G. Z. Mashanovich, V. M. N. Passaro, G. T. Reed, and O. L. Muskens, "Device-level characterization of the flow of light in integrated photonic circuits using ultrafast photomodulation spectroscopy," *Nature Photonics*, vol. 9, pp. 54–60, Nov. 2014.

[59] "National Instruments." http://www.ni.com/labview/.